ISTANBUL TECHNICAL UNIVERSITY ★ GRADUATE SCHOOL OF SCIENCE ENGINEERING AND TECHNOLOGY

REALISTIC MICROWAVE BREAST MODELS THROUGH T1-WEIGHTED 3-D MRI DATA

M.Sc. THESIS

Ahmet Hakan TUNÇAY

Department of Electronics & Communication Engineering

Biomedical Engineering Program

Thesis Advisor: Prof. Dr. İbrahim AKDUMAN

JANUARY 2013

ISTANBUL TECHNICAL UNIVERSITY ★ GRADUATE SCHOOL OF SCIENCE ENGINEERING AND TECHNOLOGY

REALISTIC MICROWAVE BREAST MODELS THROUGH T1-WEIGHTED 3-D MRI DATA

M.Sc. THESIS

Ahmet Hakan TUNÇAY
(504101401)

Electronics & Communication Engineering Department

Biomedical Engineering Program

Thesis Advisor: Prof. Dr. İbrahim AKDUMAN

JANUARY 2013

İSTANBUL TEKNİK ÜNİVERSİTESİ ★ FEN BİLİMLERİ ENSTİTÜSÜ

T1-AĞIRLIKLI 3-BOYUTLU MRI DATASI KULLANILARAK GERÇEKÇİ MİKRODALGA MEME MODELLERİ GELİŞTİRİLMESİ

YÜKSEK LİSANS TEZİ

Ahmet Hakan TUNÇAY
(504101401)

Elektronik ve Haberleşme Mühendisliği Ana Bilim Dalı

Biyomedikal Mühendisliği Programı

Tez Danışmanı: Prof. Dr. İbrahim AKDUMAN

OCAK 2013

Ahmet Hakan TUNÇAY, a **M.Sc.** student of ITU **Graduate School of Science Engineering and Technology,** student ID **504101401**, successfully defended the **thesis** entitled "**REALISTIC MICROWAVE BREAST MODELS THROUGH T1-WEIGHTED 3-D MRI DATA**", which he prepared after fulfilling the requirements specified in the associated legislations, before the jury whose signatures are below.

Thesis Advisor :	**Prof. Dr. İbrahim AKDUMAN** İstanbul Technical University	.....
Jury Members :	**Prof. Dr. İnci ÇİLESİZ** İstanbul Technical University	.....
	Prof. Dr. M. İrşadi AKSUN Koç Univeristy	.....

Date of Submission: 17 December 2012
Date of Defense: 22 January 2013

To my spouse and my parents,

FOREWORD

I would like to thank my advisor, Prof. Dr. İbrahim AKDUMAN, and declare my gratitude for all the support and knowledge he has provided me since the day I've started my Masters degree.

In particular, I would like to thank my wife for her love and patience during the periods I spent most of the time on my work and for her understanding as to my absence from home.

I also would like to thank my parents for having faith in my will and success, and being supportive and reassuring at all times.

January 2013

Ahmet Hakan TUNÇAY
(Electrical and Electronics Engineer)

TABLE OF CONTENTS

Page

ABBREVIATIONS

MRI	**:** Magnetic Resonance Imaging
GMM	**:** Gaussian Mixture Model
FDTD	**:** Finite Difference Time Domain
ACR	**:** American College of Radiology
Pdf	**:** Probability Density Function
ROI	**:** Region of Interest

LIST OF TABLES

Page

LIST OF FIGURES

Page

MICROWAVE BREAST MODELS THROUGH T1-WEIGHTED 3-D MRI DATA

SUMMARY

Biomedical microwave imaging of the human breast emerged as an important multidisciplinary research subject concerning bio-electromagnetics and signal processing. Recent years, early detection of breast cancer in the field of electromagnetic imaging has gained high popularity. In this context, computational electromagnetic models of the human breast are used to help researchers develope better techniques and instruments for imaging, increasing the feasibility of new technologies, and doing fast experimental analysis. There are hundreds of publications on the subject, which in turn stimulates the development of realistic breast phantoms for electromagnetic simulations. The increased interest in breast phantoms resulted in realistic 3-D breast phantoms derived from T1-weighted 3-D MRI data. However, development of numerical 3-D breast phantoms is still open to improvements in many areas such as effective filtering of MRI data, tissue classification, phantom shape and electromagnetic properties mapping. In this study, an effective and automated methodology for realistic numerical 3-D breast phantom development of different shapes, size and radiographic density in order to be used for different electromagnetic simulation models in microwave breast imaging research is presented. The spatial information of heterogeneity of the breast structure is collected from T1-weighted MRI slices of different patients' in prone position with normal breast tissue (not malignant or abnormal). Then each voxel in MRI data is mapped to the appropriate dielectric properties using several steps. Our work involves the processing of each MRI slice separately and combining the processes to get efficient results. First, bias field appears on each slice was estimated and eliminated by fitting a surface to the adipose voxels disrupted by the field using thin plate spline method, and then this corruptive signal was removed from the corresponding images represented by MRI data. After filtering of all slices, voxels belong to adipose and glandular tissues were classified into four categories. Utilizing the natural shape of the breast MRI histogram, they were segmented according to their intensities by a curve-fit-based segmentation method. Then those tissue categories which are represented by five MRI voxel intensity intervals were combined together and were related to electromagnetic properties of relative permittivity and conductivity by a nonlinear mapping function which is formed using monotone piecewise polynomial cubic Hermite interpolation. Electromagnetic properties of the breast tissue are expanded to desired frequency using Debye dispersion models. Each voxel intensity value is nonlinearly mapped to the appropriate electromagnetic properties of the corresponding breast tissue. Later, the resultant slices of permittivity and conductivity are linearly interpolated to form a proper 3-D breast structure. Proposed method allows transforming any axial T1-weighted 3-D MRI breast data into conductivity and permittivity distributions for a desired operating frequency with a desired grid size in order to be used in numerical microwave experiments.

.

T1-AĞIRLIKLI 3-BOYUTLU MRI DATASI KULLANILARAK GERÇEKÇİ MİKRODALGA GÖĞÜS MODELLERİ ÜRETİLMESİ

ÖZET

Meme kanseri kadınlar arasında en sık teşhis edilen kanser türüdür. Kadınlar arasında, teşhis edilen tüm kanser vakalarının yaklaşık dörtte birini meme kanseri oluşturmaktadır. Yine kadınlar arasında kansere bağlı ölümlerin yaklaşık yedide birinin meme kanseri sonucu gerçekleştiği görülmektedir. Kanser vakaları arasında bu denli öneme sahip olan meme kanserinin erken teşhisi, hastaların yaşam sürelerini kayda değer bir biçimde artırmada ilk ve en yüksek öneme sahip husustur. Non-invazif meme kanseri vakalarında kanser tedavi edildikten sonra hastanın on beş yıldan fazla yaşama olasılığı %90'ın üzerindedir. Yaklaşık olarak aynı hayatta kalma olasılığı, tümörün bir santimetreden daha küçük boyutlarda iken teşhis edilmiş olduğu invasif meme kanseri vakalarında da görülebilmektedir. Ne yazık ki, tümörün teşhis edilmesinin gecikmesi ve tümör boyutlarının iki santimetreyi aşması durumunda, tedavi sonrasında hayatta kalma olasılığı %75'lere kadar düşmektedir. Yapılan çalışmalarda, teşhis edilen tümörün boyutlarındaki bir milimetrelik artış, ölüm oranını %1.3 artırmaktadır. Bu sebeple, meme kanserine karşı en etkin savaşma biçimi şu an için erken teşhis olarak kabul görmektedir.

Meme kanserinin erken teşhisinde birçok tıbbi ve biyomedikal yöntem kullanılmaktadır. Bunlar arasında hastaların kendi kendilerine veya bir hekim tarafından yapılan el ile muayene, ultrasonografi, MRI görüntüleme ve mamografi yöntemleri ilk sırada gelmektedir. Ayrıca, yukarıdaki teşhis amaçlı yöntemlerin haricinde, çeşitli genetik incelemeler sonucunda bireylerin meme kanserine yakalanma riski de belirlenebilmektedir. Ancak, henüz hiçbir teşhis yöntemi göğüs kanserini yeterince erken teşhis edememektedir. Üstelik tüm teşhis yöntemlerinin kendilerine has zararları ve dezavantajları bulunmaktadır. Örneğin, meme kanserinin teşhisi için en yaygın kullanılan yöntem olan mamografi, tümörlerin %10 kadarını tespit edememektedir. Buna ek olarak, mamografi iyonize edici X-ışınlarını temel alarak çalıştığından, bir yandan meme kanserini tespit etmeye çalışırken diğer bir yandan meme kanserine yol açmaktadır. Bu sebeple son yıllarda meme kanserinin erken teşhisi için elektromanyetik görüntüleme yöntemlerinin kullanımı konusundaki çalışmalar hız kazanmıştır.

İnsan memesinin biyomedikal mikrodalga teknikleri kullanılarak görüntülemesi bio-elektromanyetik ve sinyal işleme ile ilgili birçok alanı içeren çok disiplinli bir araştırma konusu olarak ortaya çıkmıştır. Son yıllarda, meme kanserinin erken teşhisi konusunda mikrodalga görüntüleme alanında yapılan çalışmalar popülerlik kazanmıştır. Bu bağlamda, insan memesinin elektromanyetik sayısal modelleri bu konuda çalışan araştırmacılara, hızlı deneysel analizler yaparak yeni teknolojilerin fizibilitesinin artırılması ve böylece daha iyi görüntüleme tekniklerinin ve aygıtlarının geliştirilmesi konularında yardımcı olmaktadır. Bu konuda yayınlanmış

yüzlerce çalışma, zaman içerisinde mikrodalga meme görüntülemesi alanında sayısal meme modellerinin geliştirilmesini teşvik etmiştir.

Mikrodalga meme görüntüleme alanında ortaya konan ilk sayısal meme modelleri anatomik açıdan gerçekçilikten uzak, boşluklar ve homojen-heterojen dağılımlar içeren basit yapılı iki-boyutlu modellerdir. 1990'lı yılların başlarında ortaya çıkan bu tip modeller gerek yapısal, gerekse işlevsel açılardan büyük farklılıklar göstermekteydi. İlerleyen süreçle birlikte mikrodalga meme görüntülemesi alanına yönelik artan yoğun ilgi neticesinde, sayısal meme modellerine gösterilen önem de paralel bir şekilde artmıştır. Bu sayede bir sonraki adım olarak ortaya çıkan görece basit yapılı 3-boyutlu meme modelleri de literatürdeki çalışmalar arasında yerini almıştır. Meme modelleri konusuna gösterilen yüksek ilgi, MRI verisi kullanılarak oluşturulan anatomik açıdan gerçekçi 3-boyutlu sayısal meme modellerinin geliştirilmesiyle sonuçlanmıştır. İlk gerçekçi 3-boyutlu sayısal meme modeli kapsamlı bir çalışma ve kullanılabilir bir yöntem ile birlikte 2008 yılında ortaya konmuştur. Literatürde özel olarak sayısal mikrodalga meme modellerini konu alan bu ilk çalışmada arzu edilen türde bir model üretilebilmesi için 3 ana adım içeren bir yöntem öne sürülmüştür. Bu yöntemin alt adımları kısaca: MRI verisindeki gürültünün homomorfik filtreleme ile giderilmesi, dokuların Gauss Karışım Modeli (GMM) ile segmentasyonu ve elektromanyetik özelliklerin parçalı-doğrusal eşleme fonksiyonları ile eşlenmesi olarak tarif edilebilir.

MRI verisindeki gürültünün giderilmesi için kullanılan homomorfik filtreleme yöntemi MRI verilerinin karakteristiğine uygun bir yöntem olmayıp, genel bir gürültü giderme yöntemidir. Bu sebeple homomorfik filtreleme MRI verisindeki gürültüden kurtulmak için doğru bir yöntem değildir. Aynı şekilde GMM birleşik Gauss eğrilerinin ayrıştırılmasına ilişkin bir yöntem olup, birçok göğüs tipinde, özellikle çok yağlı göğüslerde, dokuların segmentasyonu sürecinde başarısız olmaktadır.

Elektromanyetik özelliklerin parçalı-doğrusal eşleme fonksiyonları ile eşlenmesi literatürde bugüne kadar sunulmuş olan doğrusal eşleme ve bi-modal eşleme yöntemlerine göre çok daha üstün bir yöntem olsa da, eşleme fonksiyonunun doğrusal parçalarının oluşturtulabilmesi için literatürde zaten sınırlı sayıda bulunan ve dokuların elektromanyetik özelliklerini konu alan çalışmalardaki meme dokusuna ilişkin elektromanyetik değerlerin pek de sağlıklı olmayan yollarla parçalara ayrılması gerekmektedir. Bu da elektromanyetik özelliklerin sağlıklı bir şekilde eşlenmesinin önünde bir engel teşkil etmektedir.

Tüm bunlara ek olarak halen literatürde memenin şekilsel özelliklerini tam anlamıyla yansıtan gerçekçi sayısal meme modelleri bulunmamaktadır. Mevcut 3-boyutlu modellerin gerçeğe en yakın olanları da z ekseninde sıkıştırılmış elipsoitlerin koronal kesitler halinde birleştirilmesiyle oluşturulmuş modellerdir.

Tüm bu bilgilerin ışığında şu kesin olarak söylenebilir ki, 3-boyutlu sayısal meme modelleri MRI verisinin etkin bir şekilde filtrelenmesi, doku sınıflandırılması, sayısal modellerin yapısal şekli ve elektromanyetik özelliklerin eşlenmesi gibi birçok alanda geliştirilmeye açık durumdadır.

Bu çalışmada, mikrodalga meme görüntülemesi çalışmalarında kullanılmak üzere değişik şekil, ebat ve radyografik yoğunluklarda 3-boyutlu sayısal mikrodalga meme modelleri üretilmesi için etkin ve kendi kendine işleyebilen bir yöntem sunulmuştur. Memenin heterojen yapısının mekânsal bilgisi, memelerinde bir anomaliye rastlanmayan değişik hastaların yüz üstü pozisyonda alınmış T1-ağırlıklı 3-boyutlu

MRI verileri kullanılarak elde edilmiştir. Ardından MRI verilerindeki her bir voksel değeri birçok adım sonunda uygun dilelektrik özellikler ile eşlenmiştir. MRI verisindeki kesitler önce ayrı ayrı işlenmiş, ardından tüm işlemler birleştirilerek gerçekçi sayısal modeller üretilmiştir.

İlk olarak, her bir kesitte, görüntüdeki bozucu etki olan bias alanı ince tabaka kama modeli yöntemi kullanılarak kestirilmiş ve ilgili MRI kesitinden temizlenmiştir. Bias alanının kestirimi, yağ dokulara ait örnek voksellerin toplanması ve bu voksellerin yoğunluk değerlerinin karşılaştırılması neticesinde bu örneklerden geçen ve bias alanının yumuşak değişimini temsil eden iki boyutlu bir kama modeli uydurularak gerçekleştirilmiştir. Elde edilen kestirilmiş gürültü, ilgili gürültülü kesitlerden basit bir bölme işlemi ile uzaklaştırılmıştır. Böylece gürültüden arındırılmış meme MRI verisi segmentasyon için hazır duruma getirilmiştir.

Her bir kesitin filtrelenmesinin ardından, MRI histogramının doğal şekli kullanılarak eğri uydurma tabanlı bir segmentasyon algoritması geliştirilmiş ve MRI voksel değerleri glandula ve yağ doku olmak üzere iki farklı sınıfa ayrıştırılmıştır. Segmentasyon işlemi meme MRI verisi histogramının doğal şekli olan birbirine karışmış iki Gauss eğrisinin ayrıştırılması işlemidir. Birbirine karışmış durumda bulnan bu eğrilerin her biri glandula ve yağ dokuya ait voksellerin dağılımını göstermektedir. Yağ dokuya ait olan eğrinin yarı yükseklikteki tam genişliği saptanmış ve geliştirilen algoritma ile yağ dokuyu temsil eden eğriye en iyi şekilde uyacak bir Gauss eğrisi hesaplanmış ve iki farklı doku tipini birbirinden ayıran bir eşik değeri bulunmuştur. Ardından yağ ve glandula dokularına ait voksel yoğunluk değerleri literatürdeki çalışmalar doğrultusunda sınıflandırılarak dört ana sınıfa ayrılmıştır.

Dokulara ait her bir sınıf ile elektromanyetik özellikler arasında tekdüze parçalı kübik Hermitte interpolasyon yöntemi kullanılarak doğrusal olmayan bir ilişki kurulmuştur. İlgili meme dokularının elektromanyetik özellikleri Debye and Cole-Cole dağılım modelleri üzerinden tercih edilen çalışma frekansına göre belirlenmiş, böylece MRI verisindeki her bir voksel değeri uygun bağıl geçirgenlik ve iletkenlik değerleri ile eşlenmiştir.

Bağıl geçirgenlik ve iletkenlik dağılımlarına dönüştürülen MRI kesitleri, doğrusal interpolasyon ile 3-boyutlu ve gerçekçi bir yapıya dönüştürülmüştür. Sunulan meme modeli geliştirme yöntemi, herhangi bir 3-boyutlu T1-ağırlıklı MRI verisini, tercih edilen frekanslardaki bağıl geçirgenlik ve iletkenlik dağılımlarına dönüştürerek anatomik açıdan gerçekçi 3-boyutlu sayısal mikrodalga meme modeline dönüştürmektedir.

1. INTRODUCTION

Cancer is a term used for a broad group of various diseases in which abnormal cells grow without control forming malignant tumors and are able to invade other tissues. Cancer cells may also spread to other parts of the body through the blood and lymph systems. There are also some types of tumors, known as benign, that are not cancerous. In contrast to malignant tumors, these types of tumors, what are not able to spread to other organs and do not grow uncontrollably, are usually considered as harmless cystic forms. There are more than 200 different types of cancer and 60 different organs in the body where a cancer can develop [3]. Female breast is one of the organs in which both malignant and benign tumors appear frequently. Most of the time, tumors emerges in glandular tissue which consists of lobules (milk-producing glands) and milk ducts. Glandular tissue is rich in blood vessels and lymph nodes and vessels are really close to it. Therefore, there is a high chance that the cells could have gotten into the bloodstream and spread (metastasized) to other sites in the body.

Based on the GLOBOCAN 2008 estimates, about 12.7 million cancer cases and 7.6 million cancer deaths are estimated to have occurred in 2008 [1]. Among these, breast cancer is the most frequently diagnosed cancer and the leading cause of cancer death among females, accounting for 23% (1.38 million) of the total cancer cases and 14% (458,400) of the cancer deaths [2]. Moreover, it is reported that the incidence of the cancer is rising by 0.5% annually resulting in 1.35 to 1.45 million new cases by 2010.

Early detection of breast cancer increases the lifetime of the patients severely. For non-invasive breast cancers, the survival rate after 15 years is greater that 94%. Invasive cancers of smaller than 1cm, reduces the survival rate to 90-92%, while for cancers of 1-2cm size, it remains around 75%. The death rate is increased 1.3% per millimeter increase in cancer size [5]. Therefore, early breast cancer detection is a vital subject to increase the survival preventing deaths by metastasis. There are several techniques used for early breast cancer detection including clinical and self-

breast exams, genetic screening, ultrasound, and magnetic resonance imaging and mammography.

Clinical and self-exams involve either feeling the tumor by touch or by observing the lumps or abnormalities appear on the shape. Self-exams are recommended for all women to do frequently, because it is cheap and easy to be done without going to a clinic or an hospital. However, research findings show that small cysts cannot be detected by clinical or self-exams, because when a cyst is large enough to be found, it is likely to have been growing for several years [6].

Genetic screening may help to identify people who are at increased risk for breast cancer, and also allow for specific screening of those people or their family members. It is based on investigating any mutation or abnormalities in either the two genes which susceptible for breast cancer, named BRCA1 (Breast Cancer gene one) and BRCA2 (Breast Cancer gene two). Women, who inherit any mutations or abnormalities in their BRCA genes, tend to develop breast or ovarium cancer more than the average [7]. However, genetic screening is not a method for early breast cancer detection, indeed, preserves the risk table for patients helping them to be conscious of their cancer risk.

Ultrasound is another technique that is frequently used in breast cancer detection but, not used on its own as a screening test for breast cancer. Rather, it is used to complement other screening tests. If an abnormality is seen on mammography or felt by physical exam, ultrasound is the best way to categorize it.

MRI imaging is a technique has a high soft tissue contrast and used in breast cancer diagnosis frequently. MRI imaging does not use any radiation, since less harmless than mammography. However, the cost of a typical MRI imaging season limits the usage of this technique. Although MRI is very effective at spotting abnormalities like tumors, that sensitivity can result in a false-positive reading. Currently, a breast MRI is usually ordered after a mammogram has come back showing suspicious lumps, bumps, or other abnormalities. Today, the most common screening method for breast cancer is mammography. In women who have breast screening, most cancers are found at an early stage when there is a good chance that treatment will be successful. Women who take part in breast screening reduce their risk of dying from breast cancer. In women who have breast screening, any cancer is more likely to be found early. This means that the cancer is likely to be small and more likely to be

removed by a lumpectomy (removal of the lump) rather than needing a mastectomy (removal of the whole breast). However, It is important to understand that mammography can miss 10% of the cancers. It is less sensitive in dense breasts which are seen in young women or women taking hormone replacement therapy, and this is a major disadvantage, and it is for this reason that mammography is not routinely recommended for screening for women below 40 years of age. In addition, mammograms can be uncomfortable or even painful for some women, because compressing the breast is necessary to flatten and reduce the thickness of the breast. The x-ray beam should penetrate as few layers of overlapping tissues as possible. From start to finish, the entire procedure takes about 20 minutes and the sensation can last for minutes. Another disadvantage of mammography is the radiation dose. Since mammography is an X-ray based imaging method, it is ionizing. The radiation dose for a standard two-view examination of both breasts is approximately 4.5 mGy. At first glance, it seems to be a relatively small amount of radiation dose, however it is the same with the dose that the human body can be exposed by the environment within 3 months. According to the scientists in University of Toronto, incidence of breast cancer caused by mammographic radiation for the women who were screened annually from age 40 to 55 years and biennially thereafter to age 74 years, is predicted as approximately 0.086 percent, which is also remarkable [8].

To date, there no accurate method has been proposed for early breast cancer detection. Most of the frequently used methods are usually preferred to be used together to get accurate results. Among them, mammography is the most popular method for breast cancer detection although its side effects. It is usually performed for the first diagnostic method at the beginning of the breast cancer detection procedure.

Nowadays, scientists are focused on the area "microwave imaging", because of its potential of preserving a significant and steady contrast between malignant and normal breast tissues. Previous studies on electromagnetic properties of biological tissues, and especially those of concerning the breast tissues, showed that there is a significant contrast difference between malignant and normal breast tissues from the perspective of dielectric properties [9]-[14]. In the last two decades, the number of electromagnetic therapy and diagnosis studies for the human female breast cancer is drastically increased. With the growing interests on the electromagnetic imaging of

the human breast for early cancer detection, and the electromagnetic therapy of malignant breast tumors, dozens of studies published. Several imaging methods such as microwave tomography, ultrawideband radar, narrow and wide-band microwave techniques [15]-[17]; ultrawideband radar and other time-domain techniques, such as time reversal [18]-[20]; microwave-induced thermoacoustic tomography [21]; and microwave holography [22]; proposed. Additionally, therapeutic methods such as microwave-induced hyperthermia and microwave ablation [23]-[27]; have been reported recently. At development stages of new imaging and therepathic methods, numerical models are frequently used in microwave simulations. In this context, numerical breast phantoms are served as invaluable experimental tools for biomedical electromagnetic imaging, electromagnetic therapy and all the fields of those deal with interactions between human breast tissue and the electromagnetic waves.

1.1 Purpose of Thesis

In this study, development of a general and versatile method for generating various numerical microwave breast models is aimed. Spatial information of tissue distribution is obtained from T1-wighted 3-D MRI data provided by Marmara University Medical Faculty and Euromed Medical Center. In contrast to uniform, piecewise linear and bimodal mapping methods, spatial information obtained from MRI data is mapped to the appropriate dielectric properties through non-linear mapping functions. An effective histogram based segmentation method is presented for development of numerical breast phantoms. Human dependency of the previous methods are substantially eliminated allowing to easily develop numerous numerical breast phantoms with various types for such studies in which plenty of different phantoms are required, such as neural networks algorithms.

1.2 Literature Review of Microwave Breast Models

In earlier studies, numerical breast phantoms were relatively simple, in which the heterogeneity of the breast is obtained by simple structures [28],[29]. At the beginning of 2000's more realistic numerical phantoms are derived using the spatial information of the breast tissues preserved by MRI data [30],[31]. This new development technique is based on mapping of electromagnetic properties of certain

breast tissues to the appropriate voxel intensities in MRI data. In years, with the new candidate studies on diagnostic and therapeutic microwave techniques, three different mapping methods are proposed: uniform, bimodal and piecewise-linear mapping. However, numerical phantoms were still limited to anatomically realistic 2-D phantoms or relatively simple 3-D phantoms. There had been no such study that specifically deals with 3-D anatomically realistic numerical breast phantoms until the most recent one proposed by University of Wisconsin [32]. It introduced three main stages of anatomically realistic numerical phantom development process as denoising of MRI data, segmentation of tissues and mapping of electromagnetic properties. It suggests using homomorphic filter to remove the slowly changing gradient on MRI data and two-component Gaussian Mixture Model (GMM) for segmentation of tissues.

Eventually, anatomically realistic phantoms still have deficiencies and the studies have done on this area so far pave the way for better techniques for development of numerical phantoms to use in computational electromagnetic experiments. In this context, alternative steps for development of numerical realistic 3-D breast models in order to use in biomedical electromagnetic breast cancer detection and treatment experiments is presented. T1-wighted 3-D MRI data is used for the source of spatial information of tissue distribution. Anonymous MRI samples are provided by Marmara University Medical Faculty and Euromed Medical Center. 3-D phantoms with heterogeneously distributed relative permittivity and conductivity properties vary with the spatial locations are developed. An effective noise reduction technique depends on estimating and removing the slowly changing gradient on MRI images, which is called bias field, is proposed. In addition, An histogram based segmentation algorithm is developed to be used effectively for any type of breast belong to four ACR categories defined by American College of Radiology [33]. For the first time a nonlinear electromagnetic mapping technique is integrated into development of realistic breast phantoms. In order to increase the speed of the process, MRI data is processed slice by slice, and it is stack together to form a 3-D realistic model at the end.

1.3 Basic Anatomy of the Female Breast

The main function of the breast is producing milk and feeding the baby. Breasts are positioned on the pectoralis muscles of the anterior chest wall, in left and right sides. The fundamental structure of the breast is considerably heterogeneous [34]. It consists of glandular, adipose, and fibroconnective tissues covered by 0.5-2mm thick skin layer [35]. The superficial tissue layer is separated from the skin by 0.5–2.5 cm of subcutaneous fat (adipose tissue). There are no muscles in the breast, but muscles lie under each breast and cover the ribs.

Each breast has 15 to 20 sections called lobes that are arranged like the petals of a daisy. Each lobe has many smaller lobules, which end in dozens of tiny bulbs that can produce milk. Thin tubes called milk ducts link all the lobes, lobules and bulbs. These ducts lead to the nipple in the center of a dark area of skin called the areola. Areola and nipple has major tasks in lactation. While nipple allows breast milk to pass to the suckling infant, sebaceous glands in areola secretes a kind of lubricant. In addition, underlying smooth muscle fibers compress the lactiferous ducts when the nipple is stimulated to allow for breastfeeding.

Adipose tissue fills the spaces around the lobules and ducts. A layer of fat surrounds the breast glands and extends throughout the breast. It gives the breast a soft consistency and protects the breast form external factors. A representative picture of the breast depicted in Fig. 1.1.

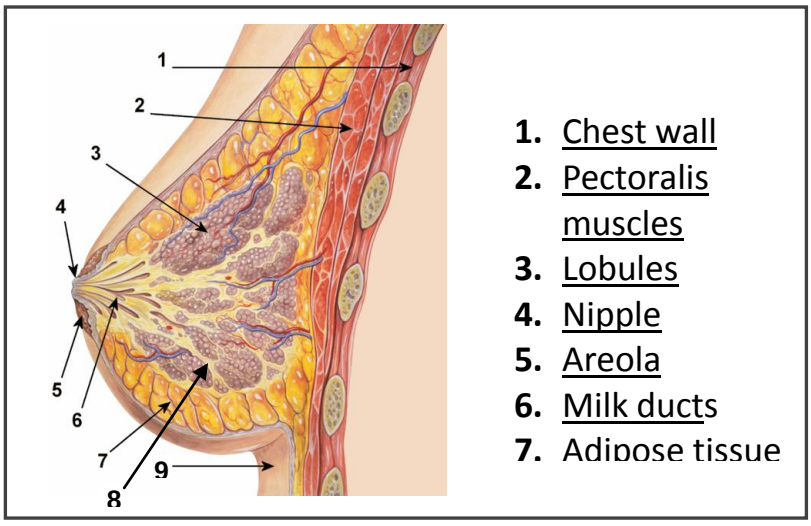

Figure 1.1 : Representative picture showing the basic anatomy of the female breast where the anatomical structures and different tissue types are indicated by numbers [46].

2. MATHEMATICAL METHODS

2.1 Thin Plate Splines

Thin plate splines were first introduced by Duchon [36] in 1976 by the physical analogy involving the bending of a thin sheet of metal plate. When it is compressed from the edges, thin metal plate deforms and bends. In order to apply this idea to the problem of coordinate transformation, one interprets the lifting of the plate as a displacement of the x or y coordinates within the plane. In 3-D coordinate system, the deflection is in the z direction and is orthogonal to the plane x-y plane.

In 2D cases, given a set of N corresponding points, the TPS warp is described by $2(N+3)$ parameters, which include six global affine motion parameters and $2N$ coefficients for correspondences of the control points. These parameters are computed by solving a linear system, in other words, TPS has closed-form solution.

Smoothing TPS is a regularized TPS. The model has a parameter p to control how non-rigid is allowed for the deformation. Given a set of control points $\{w_i, i = 1,2,\dots,N\}$, a radial basis function basically defines a spatial mapping which maps any location x in space to a new location $f(x)$, represented by,

$$f(x) = \sum_{i=1}^{K} c_i \Psi(\|x - w_i\|) \qquad \textbf{(2.1)}$$

with $\|.\|$ denotes the usual Euclidean norm, and c_i is a set of mapping coefficients, and Ψ is called the thin-plate spline basis function. Thin-plate spline basis function is defined by the length of x, given by $r = \|x\|$, as the following:

$$\Psi(x) = \|x\|^2 log\|x\|^2 \qquad \textbf{(2.2)}$$

Assume that each of N observations in $\mathbb{R}^2$ is represented by x, having the coordinates $[x\ y]^T$ and values z. Correspondingly, the sites c_i are points in $\mathbb{R}^2$. In

this case the TPS fits a mapping surface $f(x)$ between corresponding point-sets x_i, and y_i by minimizing the following energy function:

$$R(f) = \left[\iint \left(\frac{\partial^2 f}{\partial x^2}\right)^2 + 2\left(\frac{\partial^2 f}{\partial xy}\right)^2 + \left(\frac{\partial^2 f}{\partial y^2}\right)^2\right] dx\, dy \qquad \textbf{(2.3)}$$

It is also called the roughness measure, which tells how interpolated points on thin plate surge around corresponding point-set x_i, and y_i.

If the error measure $E(f)$ is define as:

$$E(f) = \sum_j \left|y_j - f(x_j)\right|^2 \qquad \textbf{(2.4)}$$

then the thin-plate smoothing spline f_{tps} is defined as the unique minimizer of the weighted sum as given below:

$$f_{tps} = \sum_{j=1}^{N} \underset{f}{argmin}(pE(f) + (1-p)R(f)) \qquad \textbf{(2.5)}$$

Here, p denotes the smoothing parameter that penalizes for curvature. With $p = 0$ there is no penalty for curvature, this corresponds to an interpolating surface function where the function passes through each observation point. At higher p values close to 1, the surface becomes smoother since curvature is penalized. For p going towards infinity the surface will go towards the plane with the least squares fit, since no curvature is allowed. It means that a proper smoothing parameter must be estimated.

According to Green and Silverman [37] f is defined in the following form in 2-D:

$$f(x) = \beta_0 + \beta_1^T \mathrm{x} + \sum_j^n \alpha_j \eta\left(\left\|x - x_j\right\|\right) \qquad \textbf{(2.6)}$$

where the η function is defined as:

$$\eta(r) = \begin{cases} r^2 log r^2 & , r > 0 \\ 0 & , r = 0 \end{cases} \qquad \textbf{(2.7)}$$

Now there are N equations, one for each observation, but there are $N+3$ variables is to be estimated; N variables α_j , one variable β_0 and two variables β_1. The last three equations from the three linear constraints:

$$\sum_{j=1}^{N} \alpha_j = \sum_{j=1}^{N} \alpha_j x_j = \sum_{j=1}^{N} \alpha_j y_j \tag{2.8}$$

that ensures that the $R(f)$ function is finite. The system can be defined in matrix form. First, the matrices

$$\boldsymbol{P} = \begin{bmatrix} 1 & \dots & 1 \\ x_1 & \dots & x_N \end{bmatrix} \tag{2.9}$$

And

$$\boldsymbol{E}_{ij} = \eta\left(\left\|x_i - x_j\right\|\right) \tag{2.10}$$

are defined. The system can then be written as:

$$\begin{bmatrix} \boldsymbol{E} + \left(\frac{(1-p)}{p}\right) I & \boldsymbol{P}^T \\ \boldsymbol{P} & 0 \end{bmatrix} \begin{bmatrix} \alpha \\ \beta \end{bmatrix} = \begin{bmatrix} Z \\ 0 \end{bmatrix} \tag{2.11}$$

where $Z = [z_1 \dots z_N]^T$, $\alpha = [\alpha_1 \dots \alpha_N]^T$,and $\beta = [\beta_0; \beta_1]$

The first line in the matrix equation is the interpolation and smoothing equations and the second line is the constraints. This matrix equation is solved with respect to α and β. An estimate of the TPS at the location x can now be calculated using equation 3.3.

To extend the formulation above to 3-D, only slight changes are needed. There are N observations in $\mathbb{R}3$, with each observation x having coordinates $[x\ y\ z]^T$ and values z. The only major change to the formulation above is that 3.4 becomes:

$$\eta(r) = \begin{cases} r\text{^}3 & , r > 0 \\ 0 & , r = 0 \end{cases} \tag{2.12}$$

The smoothing parameter p is chosen so that $\frac{(1-p)}{p}$ equals the average of the diagonal entries of the matrix $\boldsymbol{E}$, with $\boldsymbol{E} + \left(\frac{(1-p)}{p}\right) I$ the coefficient matrix of the linear system for the n coefficients of the smoothing spline to be determined. This choice of p is meant to ensure that the function is in between the two extremes; interpolation (when p is close to 1 and the coefficient matrix is essentially $\boldsymbol{E}$) and complete smoothing (when p is close to 0 and the coefficient matrix is essentially a multiple of the identity matrix). This should serve as a good first guess for p.

2.2 Some Important Features of Gaussian Distribution

Carl Friedrich Gauss invented the normal distribution in 1809 as a way to rationalize the method of least squares. Gaussian distribution function can be used when the number of events or features is extremely high. It is a continuous function approximating the accurate binomial distribution of events or features. For d dimensions, the Gaussian distribution of a vector $x = (x_1, x_2, \dots, x_d)$T is defined by:

$$N(x|\mu, \sum) = \frac{1}{(2\pi)^{\frac{d}{2}}\sqrt{|\sum|}} \, exp\left(-\frac{1}{2}(x-\mu)^T \sum^{-1} (x-\mu)\right) \qquad \textbf{(2.13)}$$

where μ is the mean and $\sum$ is the covariance matrix of the Gaussian. For example, a two dimensional Gaussian distribution with $\mu = (0,0)^T$ and $\sum = \begin{bmatrix} 0.25 & 0.30 \\ 0.30 & 1.00 \end{bmatrix}$ is illustrated in Fig. 2.1.

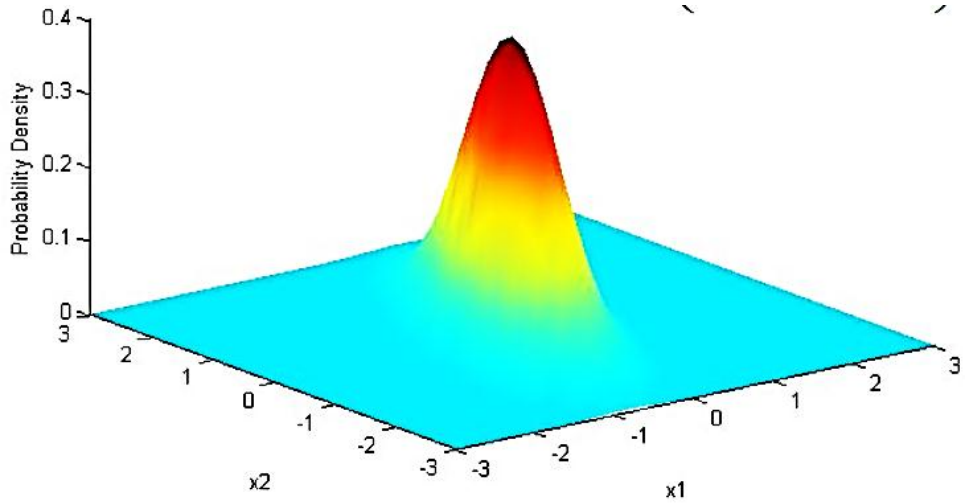

Figure 2.1 : A representative model of two-dimensional Gaussian distribution.

In one dimensional case, Gaussian distribution is defined with mean μ and standard deviation σ. The probability density function of one-dimensional Gaussian distribution is given as:

$$p(x;\mu,\sigma) = \frac{1}{\sigma\sqrt{2\pi}} exp\left(\frac{-(x-\mu)^2}{2\sigma^2}\right) \quad \textbf{(2.14)}$$

The two parameters μ and σ^2 can be shown to correspond to the mean and variance of the distribution. The shape of the Gaussian is shown in Fig. 2.2 (a) which illustrates this distribution for various σ. The significance of σ as a measure of the distribution width is clearly seen. As can be calculated from (19), the standard deviation corresponds to the half width of the peak at about 60% of the full height. In some applications, the full width at half maximum (FWHM) which is shown in (b) is often used instead. This is somewhat larger than σ and can easily be shown to be:

$$FWHM = 2\sigma\sqrt{2ln2} = 2.34\sigma \quad \textbf{(2.15)}$$

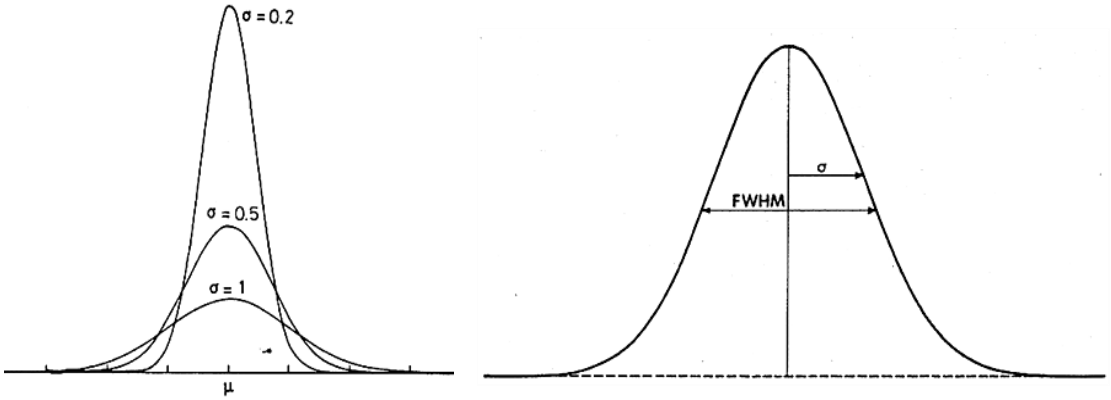

(a)

Figure 2.2 : Illustration of σ and FWHM. (a) Gaussian distribution for various σ. (b) Representation of FWHM with σ.

An important practical note is the area under the Gaussian between integral intervals of σ. This is shown in Fig. 2.3. These values should be kept in mind when interpreting measurement errors. The presentation of a result as $x \pm \sigma$ signifies, in fact, that the true value has $\approx 68\%$ probability of lying between the limits $x - \sigma$ and $x + \sigma$ or a 95% probability of lying between $x - 2\sigma$ and $x + 2\sigma$, etc. Note that for a 1σ interval, there is almost a $1/3$ probability that the true value is outside

these limits. If two standard deviations are taken, then, the probability of being outside is only $\approx 5\%$, etc.

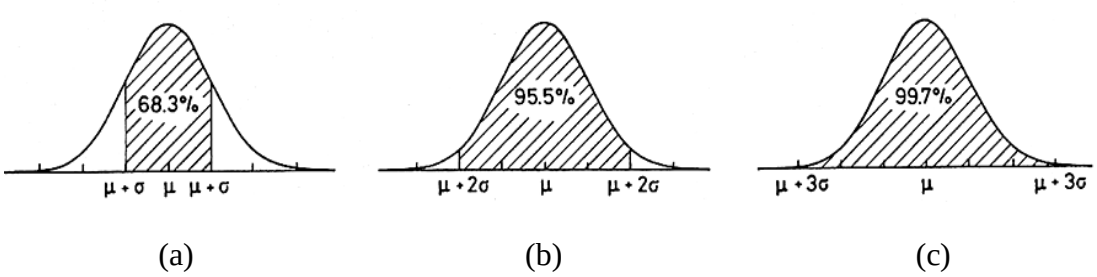

(a) (b) (c)

Figure 2.3 : The area contained between the limits $\boldsymbol{\mu \pm 1}$, $\boldsymbol{\mu \pm 2\sigma}$ and $\boldsymbol{\mu \pm 3\sigma}$ in a Gaussian distribution.

2.3 Monotone Piecewise Cubic Hermite Interpolation

Many of the most effective interpolation techniques are based on piecewise cubic polynomials. Monotone piecewise cubic interpolation is a variant of cubic interpolation that preserves monotonicity of the data set being interpolated [38], [39]. A cubic Hermite spline is a third degree spline with each polynomial of the spline in Hermite form. The Hermite form consists of two control points and two control tangents for each polynomial. Each interpolation is performed on one sub-interval at

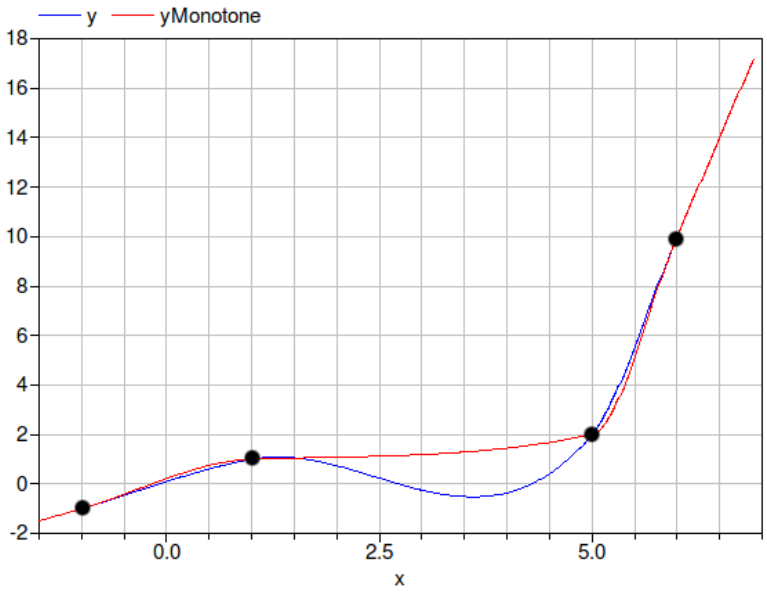

Figure 2.4 : Comparing monotone piecewise cubic Hermite interpolation (red) vs cubic Hermite interpolation (blue).

a time (piece-wise). Monotonicity is preserved by linear interpolation but not by cubic interpolation. Fig. 2.4 shows the difference between monotone piecewise cubic Hermite interpolation and cubic Hermite interpolation.

2.3.1 Cubic interpolation

Given values of the function to be interpolated f_k at $t = x_k$ and f_{k+1} at $t = x_{k+1}$, and values of the derivatives at those points, d_k at $t = x_k$ and d_{k+1} at $t = x_{k+1}$, then,

$$f(t) = h_{00}\left(\frac{t - x_k}{s_k}\right) f_k + h_{10}\left(\frac{t - x_k}{s_k}\right) s_k d_k + h_{01}\left(\frac{t - x_k}{s_k}\right) f_{k+1} + h_{11}\left(\frac{t - x_k}{s_k}\right) s_k d_{k+1} \quad \textbf{(2.16)}$$

with $s_k = x_{k+1} - x_k$ and $h_{ij}(t)$ as before, satisfies

$$f(x_k) = f_k, f(x_{k+1}) = f_{k+1}, \quad \textbf{(2.17)}$$

$$f'_+(x_k) = d_k, f'_-(x_{k+1}) = d_k + 1 \quad \textbf{(2.18)}$$

where h_{ij} are the basis functions for the cubic Hermite spline. This cubic polynomial is unique, subject to these four conditions.

2.3.2 Interpolating a data set

Suppose there are p points in some interval $[a, b]$, $a < x_1 < x_2 < \ ... < x_p < b$, and corresponding values of the function, f_k, and the derivative, d_k at each point x_k. Accordingly, $x_0 = a, x_p = b$ and f_0, f_{p+1}, d_0 and d_{p+1} can be defined. Then the piecewise cubic interpolant is going to be:

$$f(t) = \sum_{k=0}^{p} \left\{ h_{00}\left(\frac{t - x_k}{s_k}\right) f_k + h_{10}\left(\frac{t - x_k}{s_k}\right) s_k d_k + h_{01}\left(\frac{t - x_k}{s_k}\right) f_{k+1} + h_{11}\left(\frac{t - x_k}{s_k}\right) s_k d_{k+1} \right\} \quad \textbf{(2.19)}$$

with $s_k = x_{k+1} - x_k$ as before, and $h_{ij}(t) = 0$ for $t \notin [0,1]$. Then the basis functions $\phi_k(t)$,and $\varphi_k(t)$ can be introduced as:

$$\phi_k(t) = \begin{cases} h_{00}\left(\frac{t-x_0}{s_0}\right) & if\ k = 0 \\ h_{00}\left(\frac{t-x_k}{s_k}\right) + h_{01}\left(\frac{t-x_{k-1}}{s_{k-1}}\right) & if\ k = 1,\ldots,p \\ h_{01}\left(\frac{t-x_p}{s_p}\right) & if\ k = p+1 \end{cases} \quad \textbf{(2.20)}$$

$$\varphi_k(t) = \begin{cases} h_{10}\left(\frac{t-x_0}{s_0}\right)s_0 & if\ k = 0 \\ h_{10}\left(\frac{t-x_k}{s_k}\right)s_k + h_{11}\left(\frac{t-x_{k-1}}{s_{k-1}}\right)s_{k-1} & if\ k = 1,\ldots,p \\ h_{11}\left(\frac{t-x_p}{s_p}\right)s_p & if\ k = p+1 \end{cases} \quad \textbf{(2.21)}$$

and the piecewise cubic interpolant will be:

$$f(t) = \sum_{k=0}^{p+1} \phi_k(t) f_k + \sum_{k=0}^{p+1} \varphi_k(t) d_k \quad \textbf{(2.22)}$$

2.3.3 Monoton interpolation

Given $\alpha = x_0 < x_1 < \cdots < x_p < x_{p+1} = b$ and $f_0 < \cdots < f_{p+1}$, with d_ks unspecified, it's always possible to find d_ks such that the resulting $f(t)$ is strictly increasing [38]. Let

$$\Delta_k = \frac{f_{k+1} - f_k}{x_{k+1} - x_k}, \alpha_k = \frac{d_k}{\Delta_k}, \qquad \beta_k = \frac{d_{k+1}}{\Delta_k} \quad \textbf{(2.23)}$$

then $f(t)$ is monotone in $[x_k;\ x_{k+1}]$, if and only if:

1. $\alpha_k + \beta_k - 2 \leq 0$,and $sign(d_k) = sign(d_{k+1}) = sign(\Delta_k)$; or

2. $\alpha_k + \beta_k - 2 > 0$, $sign(d_k) = sign(d_{k+1}) = sign(\Delta_k)$; and:

   (a) $2\alpha_k + \beta_k - 3 \leq 0$, or

   (b) $\alpha_k + 2\beta_k - 3 \leq 0$, or

   (c) $\alpha_k - \frac{(2\alpha_k+\beta_k-3)^2}{3(\alpha_k+\beta_k-2)} \geq 0$

The condition

$$\sqrt{\alpha_k^2 + \beta_k^2} \leq 3 \tag{2.24}$$

implies either 1 or 2(a) −2(c) above, so it's sufficient to guarantee monotonicity. This motivates the following algorithm for constructing the d_ks:

1. Initialize the derivatives $\{d_k\}$ so that $sign(d_k) = sign(d_{k+1}) = sign(\Delta_k)$. For instance,

$$d_0 = \Delta_0, d_k = \frac{\Delta_{k-1} + \Delta_k}{2} \; for \; k = 1, \ldots, p, d_{p+1} = \Delta_p \tag{2.25}$$

2. For $k = 0, \ldots, p$:

(a) If $\sqrt{\alpha_k^2 + \beta_k^2} \leq 3$ the interpolant will be monotone in $[x_k;\ x_{k+1}]$; go to next k.

(b) If $\sqrt{\alpha_k^2 + \beta_k^2} > 3$, let $\tau_k = \frac{3}{\sqrt{\alpha_k^2+\beta_k^2}}$, $\alpha_k^* = \tau_k \alpha_k$, and $\beta_k^* = \tau_k \beta_k$; set

$$d_k = \alpha_k^* \Delta_k, \tag{2.26}$$

$$d_{k+1} = \beta_k^* \Delta_k \tag{2.27}$$

The interpolant will be monotone in $[x_k;\ x_{k+1}]$; go to next k. The algorithm may change the value of each d_k at most twice from its initial value: first when the interval $[x_k;\ x_{k+1}]$ is considered and again when the interval $[x_k;\ x_{k+1}]$ is considered. But since $0 \leq * \alpha_k^* \leq \alpha_k$ and $0 \leq * \beta_k^* \leq \beta_k$, the modification of d_k for $[x_k;\ x_{k+1}]$ will maintain the monotonicity condition on $[x_k;\ x_{k+1}]$.

2.4 Electromagnetic Models for Biological Tissues

Electromagnetic properties of biological tissues for different frequencies can be calculated using proper electromagnetic dispersion models such as Cole-Cole or

Debye models. Actually, both models are based on the dielectric relaxation response of dispersive materials based on the frequency.

Debye relaxation model is usually expressed in the complex relative permittivity ε_r^* of a medium as a function of the field's frequency ω. Single pole Debye dispersion expressions are given in the following form:

$$\varepsilon_r^*(\omega) = \varepsilon_\infty + \frac{\Delta\varepsilon}{1 + j\omega\tau} - j\frac{\sigma_s}{\omega\varepsilon_o} \tag{2.28}$$

Here, ε_∞ is the relative permittivity at infinite frequency, σ_s is the static conductivity, and ε_o as the permittivity of free space and τ is the relaxation time constant. the The term $\Delta\varepsilon$ is called the magnitude of the dispersion and expressed as below:

$$\Delta\varepsilon = \varepsilon_s - \varepsilon_\infty \tag{2.29}$$

where ε_s is the static relative permittivity.

The other one, Cole–Cole relaxation model is based on the same parameters used in Debye model with one except; Cole-Cole model includes a distribution parameter α, which takes a value between 0 and 1, allows to describe different spectral shapes. For the single pole Cole-Cole dispersion model, the frequency-dependent permittivity is given as:

$$\varepsilon_r^*(\omega) = \varepsilon_\infty + \frac{\Delta\varepsilon}{1 + (j\omega\tau)^{(1-\alpha)}} - j\frac{\sigma_s}{\omega\varepsilon_o} \tag{2.30}$$

As seen from the expression, when $\alpha = 0$, Cole-Cole model reduces to the Debye model.

In both cases, equations (2.28) and (2.29) can be used to predict the dielectric behavior over the desired frequency range. The corresponding equation for the tissue conductivity can be derived from the general relation between conductivity and permittivity given below:

$$\frac{(\Delta\varepsilon)\varepsilon_o}{\tau} = \sigma_\infty - \sigma_s \tag{2.31}$$

where σ_∞ is the conductivity at infinite firequency.

Consequently, the complex conductivity σ^* and the complex specific impedance z^* of the tissue can be calculated using the expressions below:

$$\sigma^* = j\omega\varepsilon_o\varepsilon^* = \sigma_\infty + \omega\varepsilon_o\varepsilon_\infty + \frac{\sigma_s - \sigma_\infty}{1 + j\omega\tau} \quad \textbf{(2.32)}$$

$$z^* = \frac{1}{\sigma^*} \quad \textbf{(2.33)}$$

3. METHODOLOGY

In this study, our purpose is to preserve an efficient method for development of 3-D realistic microwave breast models using T1-weighted 3-D MRI data to be used in microwave breast imaging experiments. The body of work can be summarized as mapping of correct electromagnetic properties to the correct spatial coordinates of the breast. 3-D MRI of anonymous patients is used to obtain the spatial information of tissue distributions inside the female breast.

The methodology can be separate into four parts as pre-processing of MRI data, bias field correction, and tissue segmentation, electromagnetic properties mapping, and building the 3-D structure. Each of them are associated with the previous one, indeed, each process prepares the data for the next step up to the end. Some of the parameters given in this paper are proportional to the size of the provided MRI data, and need to be changed according to specific studies.

3.1 Properties of MRI Data

Numerical phantoms are generated using T1-weighted 3-D MRI data. Collection of axial MRI data belonging to anonymous and non-cancerous patients is provided by Marmara University Medical Faculty in order to be used in numerical phantom development. Provided MRI data consist of 40-45 slices per patient in prone position. An example of MRI data with 42 slices is illustrated in Fig. 3.1. Each axial slice of the patients' chest consists of 1024x1024 voxels, with 8-bit grey color format. Typical field-of-view of given MRI is 32cm x 32cm and spacing between each slice is approximately 3mm. In this case, each voxel in the MRI data represents a 0.369mm x 0.369mm x 3mm volume. A more detailed view of the 20th slice of Data 1 is showed in Fig. 3.2.

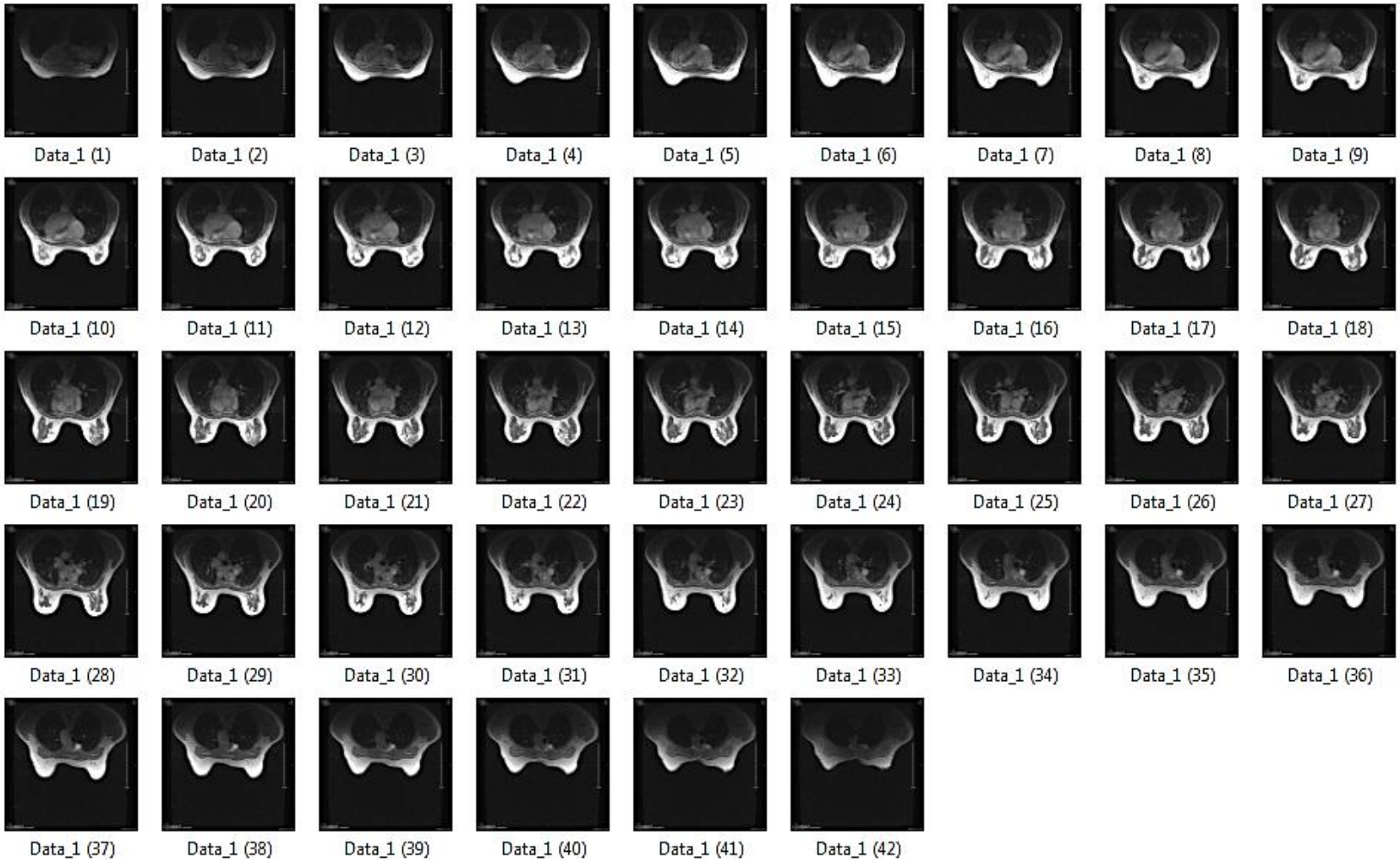

Figure 3.1 : An example of MRI data which consists of 42 slices of an anonymous patient in prone position.

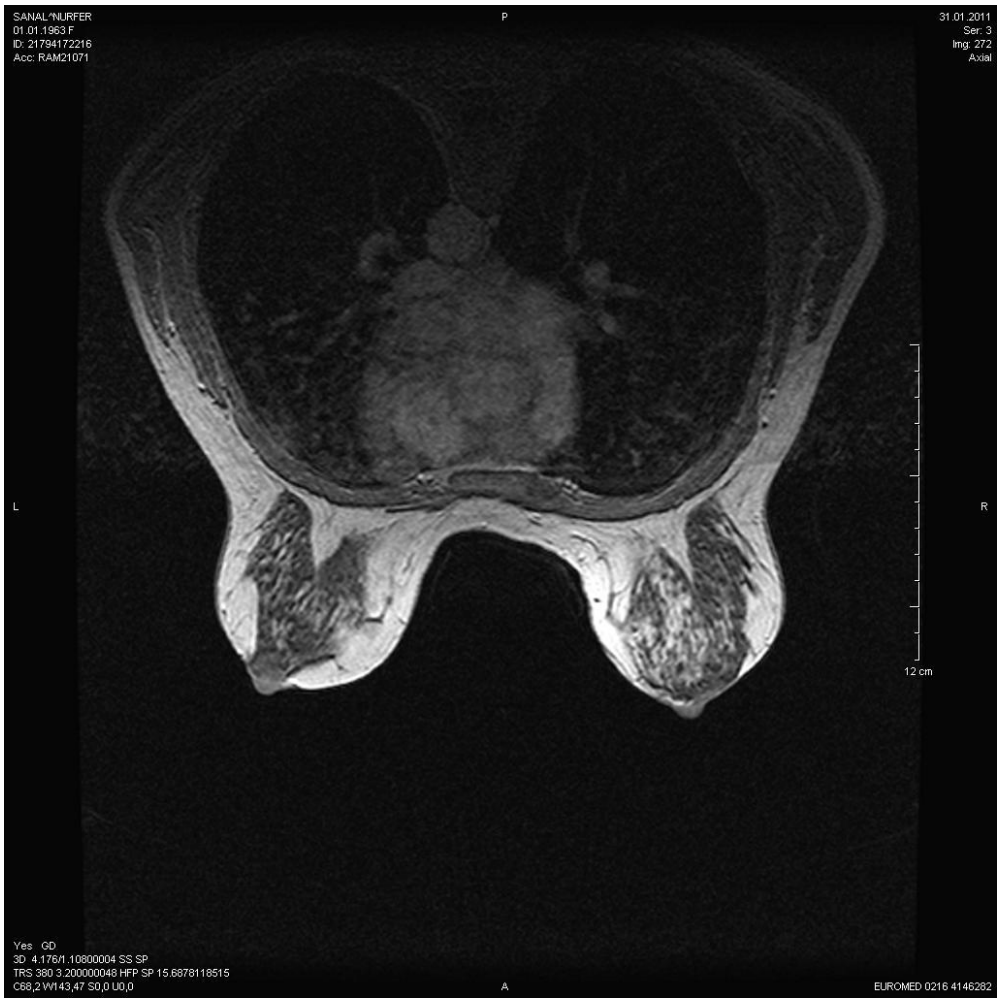

Figure 3.2 : A more detailed view of an MRI slice.

3.1.1 Pre-processing of MRI data

Provided MRI data pictures the whole chest of the patients. It covers the Therefore, the region that consists only the breast is extracted from the data. First, the breast whose electromagnetic model is going to be created is enclosed by a restrictive box as illustrated in Fig. 3.3(a). Then, the structure inside the box is extracted from the data as shown in (b). By this way, any other structures such as chest wall, internal organs etc. are removed. The size of an extracted slice varies patient to patient, but it is approximately 300x300 voxels.

Before starting development process, each slice should be interpolated to obtain required cell size for desired operating frequency, which increases the speed of the algorithm. For example, for an operating frequency of 6 GHz and 20 points per wavelength, the required grid size will be 5mm x 5mm x 5mm, which is

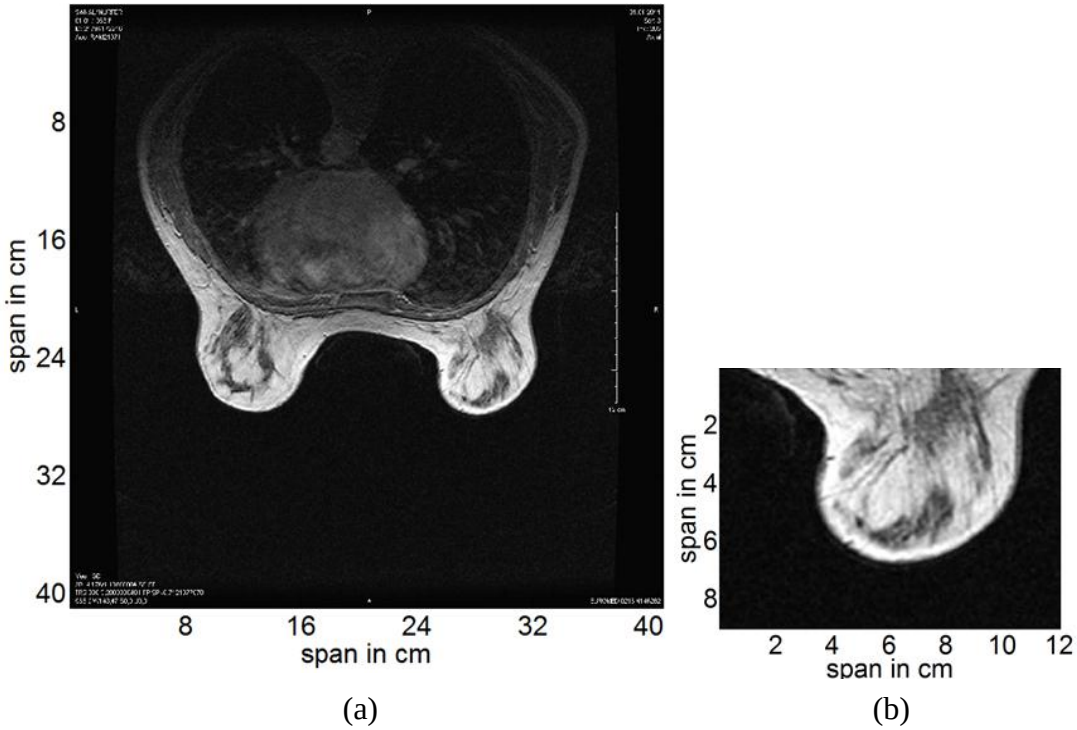

(a) (b)

Figure 3.3 : Extraction of the breast tissue from axial slices of 3-D MRI data. (a) A simple box is defined to cover whole breast tissue. (b) Breast tissue is extracted from each of the slices using the box

approximately 13.5 times the given grid size. Therefore, for an MRI data with a voxel size 0.369mm x 0.369mm x 3mm, size of each slice must be reduced by a factor 13.5, increasing the speed of the numerical phantom development process, approximately, by 10 times. However, if desired frequency or desired simulation method requires a gird size smaller than the given MRI data, than it is more reasonable to apply interpolation step just before building the 3-D structure of the numerical breast phantom.

3.1.2 Removing the background artefects

One important purpose of prepossessing of MRI data is to prepare the data for segmentation. Our segmentation method is based on the natural property of breast MRI histogram that is composed of a mixture of two Gaussians, which is fully covered in section II-C. Any noises, such as artifacts on the background, can lead inaccurate mapping of electromagnetic properties disrupting the distribution of the voxel intensities on histogram and must be removed before tissue segmentation. In fact, the artifacts are considered as a low intensity noise at the breast exterior originate from either the non-uniformities due to the bandwidth-limiting filtering

and/or the ghost images which is seen mainly in the phase direction [40]. Several image processing steps are applied to eliminate this noise seen at the exterior of the breast. Fig. 3.4(a) shows an axial slice with background artifacts which are actually barely seen. First, MRI data is multiplied by a constant to increase the contrast between the artifacts and the background. This multiplication is followed by a thresholding step using Otsu's method [41] in order to generate a binary image as shown in Fig. 3.4(b). To sever the connected components in the binary mask, it is eroded with a structural element of a radius of 2 voxels [42], [43]. Connected component with the biggest area is considered as the rough mask of the breast. All the other components are removed from the corresponding slice and reverse the erosion operation by applying dilation with the same structural element. Result is shown in Fig. 3.4 (c).

Although the resultant slices contain only the binary masks, and the noise at the environment is removed, the masks have indented boarders. As depicted in Fig. 3.4.(d), a Gaussian filter with a 8cm x 8cm kernel size with $\sigma = 3$ cm is applied to smooth the boarders by eliminating the high frequency noises. Again, final binary mask is generated by Otsu's method and is eroded by 1.5 cm in order to maintain the original size of the mask. Lastly, MRI data is multiplied with the final mask illustrated in Fig. 3.4 (e). As shown in the Fig. 3.4 (f), low intensity artifacts at the background and the skin are removed from the data preserving sharper edges and

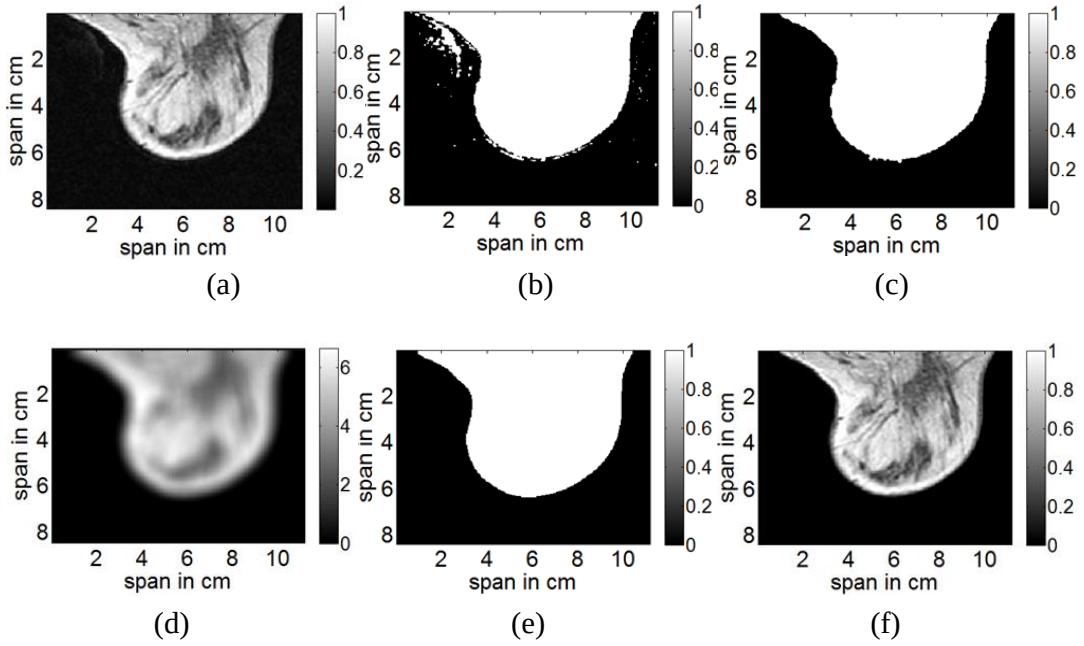

Figure 3.4 : Elimination of the noise at the breast exterior on MRI data.

uniform background. Removing the background artifacts also provides noticeable enhancement in MRI histogram. In Fig. 3.5, probability density functions of MRI voxel intensities illustrate how the masking operations and noise reduction steps explained so far effects the distribution and the shape of the voxel intensities. Pdf of the noisy MRI data is shown in Fig. 3.5(a). It can be seen that most of the voxels, which are belong to the background (thus expected to be 0), are clustered around the intensity value 0.1. As illustrated in Fig 3.5(b), initial masking (see example in Fig 3.4 (b)) sharply removes most of the salt and pepper type background noises. However, artifacts on the background still corrupt the distribution at lower intensities. These artifacts cause the sharp peak near the voxel intensities at 0.1. As depicted in Fig 3.5(c), it is eliminated by removing the connected components on the background (see example in Fig 3.4(c)). Neglecting the skin layer also enhances the distribution. Only the difference between Fig. 3.5(c) and (d) is that the skin layer is neglected in (d).

Noise reduction on the background yields remarkable enhancement especially at lower intensities, which belong to glandular tissue. However, it is not enough to reveal the mixed Gaussians in a breast MRI histogram. There is another type of noise that also corrupts the Gaussian curves in the histogram by changing the voxel intensities, called bias field. Some distinguishable disruptive effects of bias field are depicted in (d).

Removing the bias field from the breast MRI data is essential for segmentation process as well as removing the background noises. Unfortunately, removing the bias field is a tough process because it is hidden in the data. Therefore, it must be estimated before eliminated.

3.2 Bias Field Correction

Bias field in MRI images is a low frequency and smoothly changing signal that corrupts MRI images by changing voxel intensity values. This slowly changing field cross an image is caused by poor radio frequency coil uniformity and patients' anatomy inside or outside the field-of-view. Therefore bias field occurs in MRI images is unique for each patient and even each MRI imaging season. The magnitude of the variation in intensity values is typically varies between the range 10-20%

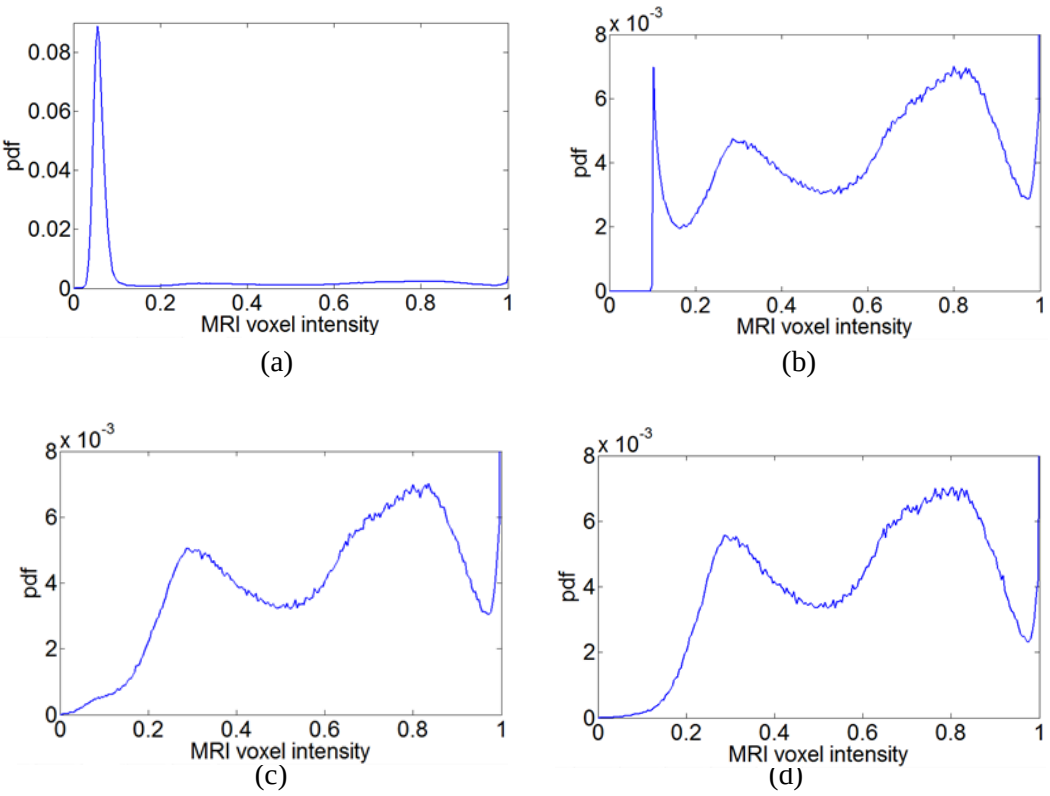

Figure 3.5 : Probability density functions of MRI voxel intensities of the same data illustrate how the masking operations and noise reduction steps effects the distribution.

resulting a tissue has not a unique voxel intensity value [44]. This means that two different tissues can have the same voxel intensity value causing confusion. This intricacy causes segmentation errors and leads inaccuracy at electromagnetic properties mapping stage. In addition, it has disruptive effects on the histogram. As mentioned before, any artifacts that corrupt the Gaussian structure of histogram lead also segmentation errors.

In the previous study [32], bias field is tried to be suppressed by a simple homomorphic filter. Homomorphic filtering is not an adaptable filtering method; instead, it is a general method, which is used for suppressing the contrast components (or background illumination) on images. However, in MRI data, bias field does not only increase the illumination on the background, but also reduce it. Thus, a simple homomorphic filtering operation does not give sufficient results on MRI images. Fig. 3.6(a) shows a breast MRI slice corrupted by a bias field and (b) resultant slice after homomorphic filtering. As seen, homomorphic filter slightly reduces the background

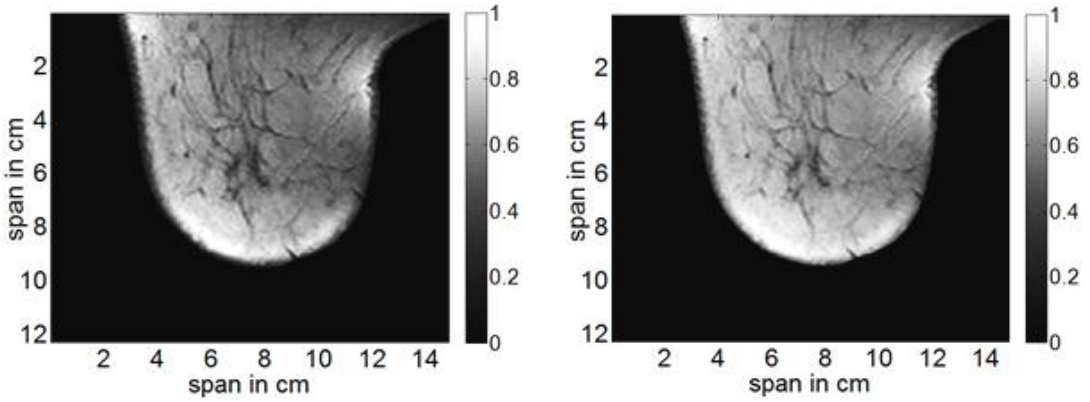

(a) (b)

Figure 3.6 : Application of homomorphic filtering on an MRI slice corrupted by a bias field.

illumination, but obviously fails on the darker regions. Instead of trying to remove the bias field from the MRI slices by simple filtering operations, estimating and modeling the bias field directly on the corresponding slice and then eliminating it is more reasonable.

Main idea of removing the bias field is lies on estimating the bias field in each slices and then removing this corruptive field from the data by a simple division. Estimation of the bias field is completed in two steps. First, enough number of the sample points (100-400 points according to the breast size) belonging to the adipose tissue in the related MRI slice are gathered. Then assuming the voxel intensities belonging to adipose tissue should have the maximum values, any subsidence in the intensity of those sample points refers to the bias field. Since bias field is a smoothly changing signal, it can be estimated by fitting a thin plate spline surface to those sample points [45].

3.2.1 Collecting the sample points

In each slice, voxels belonging to adipose tissue are taken as the local maxima inside a window that scans the ROI with some overlap. The region of interest (ROI) is defined as the smallest rectangle whose size is N_c x N_r, covering the whole breast tissue in the given MRI slice. It determines the boundaries for the scanning operation. Fig. 3.7 illustrates the ROI and the scanning operation on a sample binary y direction is given as o_c, and o_r respectively. Gathering the correct voxels belonging to adipose tissue is the vital step for a correct estimation of bias field.

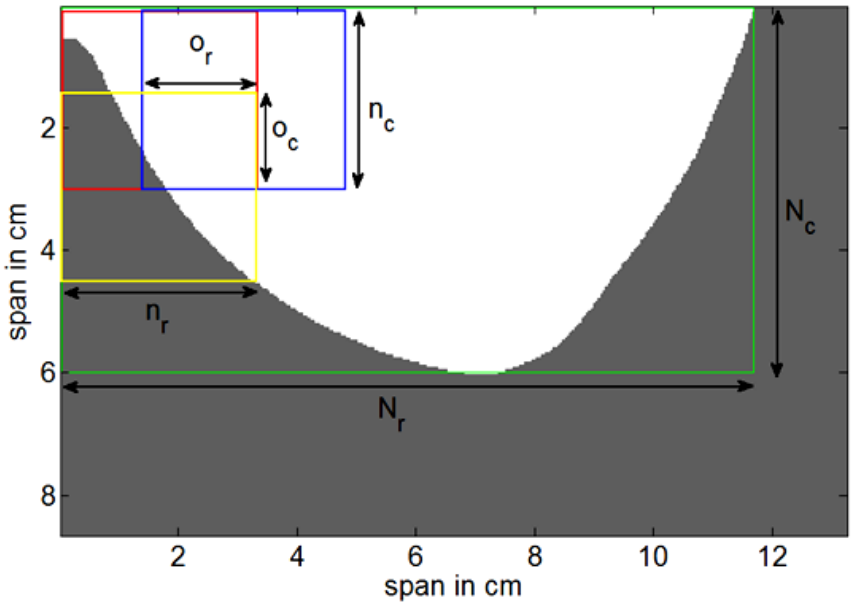

Figure 3.7 : Illustration of the ROI and the scanning operation on a representative binary mask

The distribution of the glandular tissue can lead false determination of some adipose tissues. This happens when a scanning window is fully filled with glandular tissue. In this case, the local maximum is taken as the maximum voxel intensity belonging to the glandular tissue yielding remarkably low voxel intensity. In order to avoid false determination of sample points, different window parameters (yielding different window sizes and amount of overlap) for different regions of the breast depending on the tissue distributions. As illustrated in Fig. 3.8, breast interior is divided into four different regions denoted by R_1 to R_4 depending on the distributions of glandular and adipose tissue densities.

Four different regions are defined by three thickness parameters δ_1, δ_2, δ_3 which determines the thickness of the regions R_1, R_2, R_3 respectively, and rest of the area is labeled as $R4$.

R_1 defines the region that includes nipple which is composed of milk ducts and very rich in glandular tissue. In a breast MRI of a patient in prone position, nipple is usually located at the bottom of the breast when the patient is in prone position. Therefore $R1$ is defined as the last $\delta 1$ rows at the bottom of the ROI.

The structure of the glandular tissue starts branching out from the nipple through the chest wall, and is separated from the skin by 0.5-2.5 cm of subcutaneous fat.

Therefore, the lateral edges of the breast denoted by R_2 composed of almost completely adipose tissue.

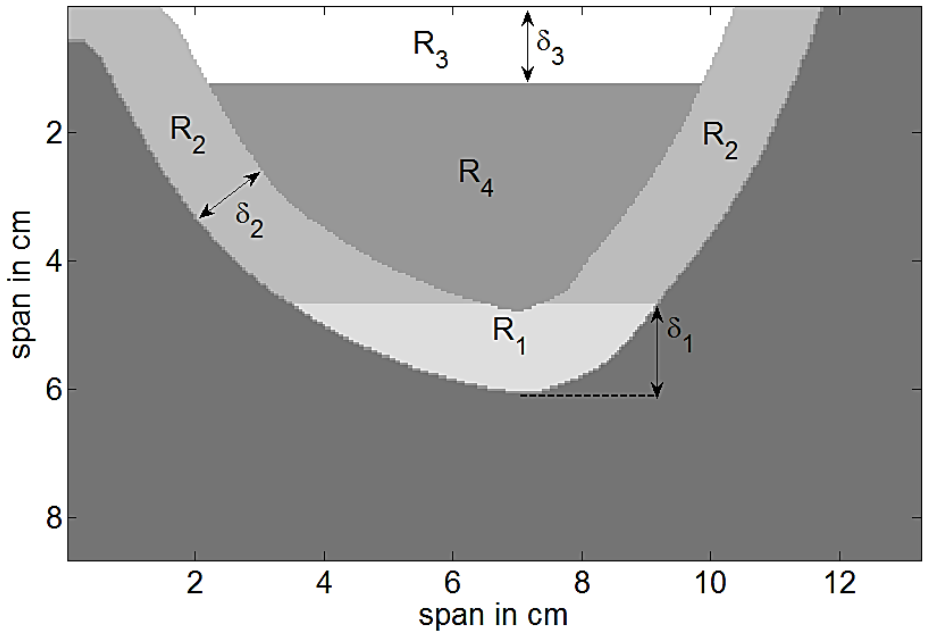

Figure 3.8 : Four different regions depending on the distributions of glandular and adipose tissue densities.

For R_1 and R_2, sizes of the windows are the same and they are relatively smaller than the windows used for R_3 and R_4. The reason is that smaller windows yield greater number of samples and gathering number of sample points near the boarders of the breast produce better estimation of bias field. Retrieved sample points from the regions $R1$ and R_2 are illustrated with red dots in Fig. 3.9. Skin layer is neglected during the screening operation excluding non-adipose voxels in order to avoid incorrect samples.

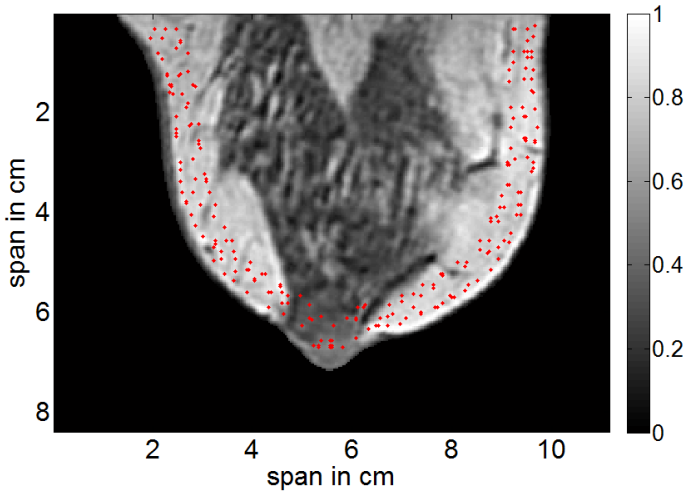

Figure 3.9 : Retrieved sample points from the regions $\boldsymbol{R_1}$ and $\boldsymbol{R_2}$

There is also another region which lies on near the chest wall and rich in glandular tissue than R_2, indicated by R_3. Local maximas found on this region are shown in Fig. 3.10. Again the window size for R_3 is the same with those for R_1 and R_2.

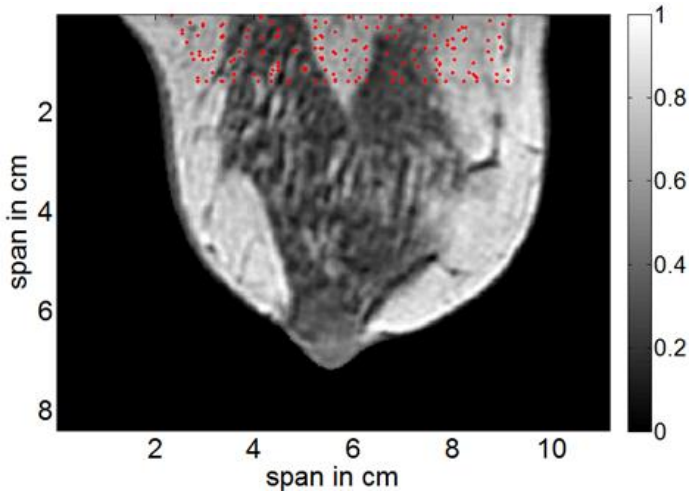

Figure 3.10 : Retrieved sample points from the regions $\boldsymbol{R_3}$.

Finally, the region confined with R_1,R_2 and R_3 is represented by R_4 which is composed of mostly the glandular tissue and has the greater area. Fig. 3.11 depicts the local maximas found in R_4. Since it may contain large amount of glandular tissue, required window size must be large enough to cover some adipose tissue.

As mentioned before, four different regions are defined by three thickness operators named δ_1, δ_2, and δ_3. δ_1 is selected as 1.5 cm which is the maximum height of the nipple area out of 20 different breast MRIs.

Other two thickness parameters are defined proportional to the size of the current slice of the breast in order to avoid the selected sample points go out of the breast

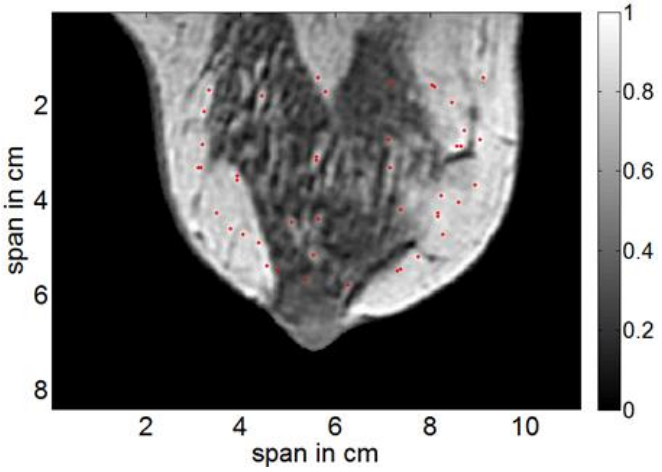

Figure 3.11 : Retrieved sample points from the regions $\boldsymbol{R_4}$.

bounds. δ_2 is taken as minimum adipose thickness just under the skin which is 5 mm (for a medium sized breast it is nearly $Nr/15$). Likewise, δ_3 is selected as 2 cm (nearly $Nc/4$) as an optimum value after examining different breast MRIs.

For each region, local maximas are retrieved using a scanning window whose parameters are peculiar to different regions. Coordinates and the values of retrieved points are stored in a matrix I_{max}. Corresponding window parameters for sampling are given in Table 1.

Table 3.1 : Corresponding window sizes for finding local maxima.

R_1	R_2	R_3	R_4
$n_{r1}=N_r/25$	$n_{r2}=N_r/25$	$n_{r3}=N_r/25$	$n_{r4}=4sN_r/25$
$n_{c1}=N_c/25$	$n_{c2}=N_c/25$	$n_{c3}=N_c/25$	$n_{c4}=4sN_c/25$
$o_{r1}=0.5n_{r1}$	$o_{r2}=0.5n_{r2}$	$o_{r3}=0.5n_{r3}$	$o_{r4}=0.5n_{r4}$
$o_{c1}=0.5n_{c1}$	$o_{c2}=0.5n_{c2}$	$o_{c3}=0.5n_{c3}$	$o_{c4}=0.5n_{c4}$

However there is a special case for R_4. In mid slices, most of the glandular tissue appear in R_4, so a bigger size scanning window should be defined to reduce undesired samples belonging to glandular tissue. On the other hand, density of the glandular tissue reduces in lateral slices. Therefore, bigger sized scanning windows lead insufficient number of samples. To overcome this problem, a parameter called the *slice factor* is defined for the region R_4, which slightly decreases the corresponding scanning window sizes up to (approximately) 4 times, in lateral slices. For a corresponding MRI data consists of K slices, slice factor s for k^{th} slice is calculated as given below:

$$s(k) = \frac{(X - s')}{max(X - s')} \quad \textbf{(3.1)}$$

where

$$s' = \left|\frac{K}{2} - k\right| + 1 \qquad , k = 1,2, \dots K \quad \textbf{(3.2)}$$

and

$$X = \frac{4\,max(s') - min(s')}{3} \quad \textbf{(3.3)}$$

Then the corresponding window sizes for each slice are divided by the slice factor yielding approximately no-change in the mid slice while 1/4 times size reduction in lateral slices (which is equal to the window size for R_1, R_2, and R_4). For example, linear change of the s in an MRI data with 42 slices is given in Fig. 3.12. Slice factor increases the number of sample voxels especially at lateral slices.

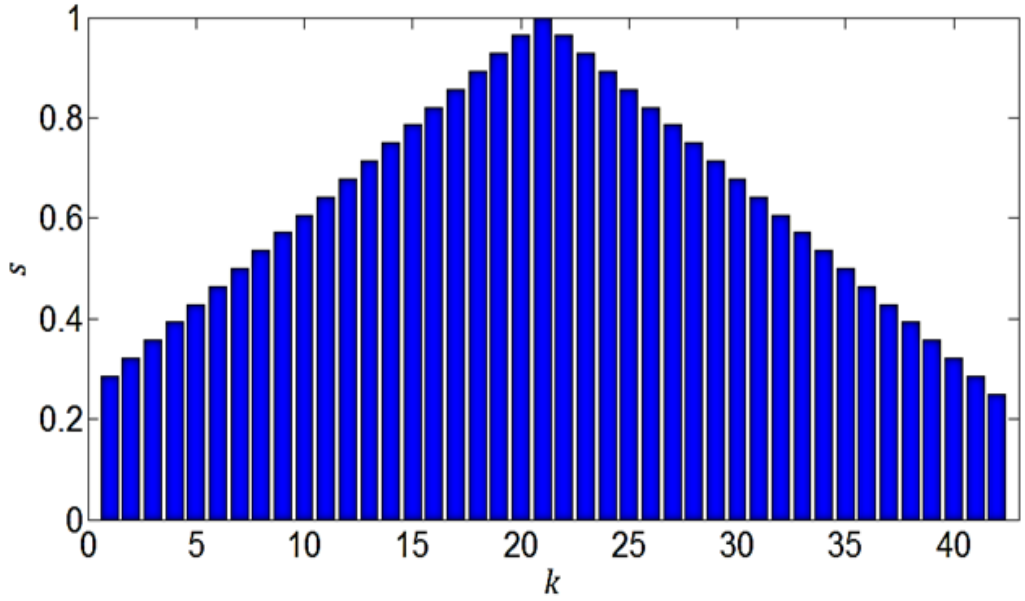

Figure 3.12 : Relation between the slice factor $\boldsymbol{s}$ and the slice number $\boldsymbol{k}$.

Fig. 3.13 represents the sample voxels collected from the same slice with and without using the slice factor. As seen in (a), bigger scanning window leads insufficient number of sample voxels in the region R_4. On the other hand, using a smaller scanning window in R_4 provides relatively large quantity of samples as depicted in (b).

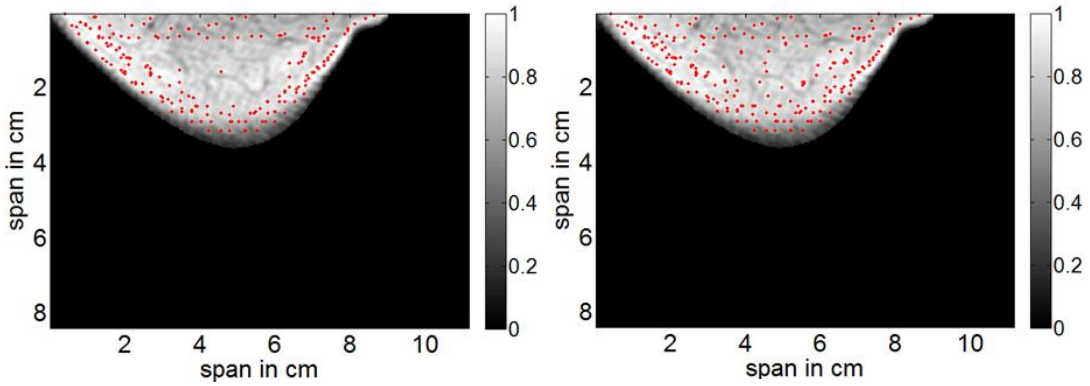

(a) (b)

Figure 3.13 : Sample voxels collected from the same slice with and without using the slice factor

3.2.2 Discarding the non-adipose voxels

Using different scanning window sizes for different regions is a clever idea which drastically reduce the number of undesired samples. However, it is not a complete solution. Fig. 3.14 (a) illustrates the selected sample voxels, which are expected to represent adipose tissue. Obviously, there are still some samples belonging to non-adipose voxels. They can be distinguished from the correct samples using the properties of bias field. Since bias field is a slowly changing signal, voxels belong to adipose tissue tent to have similar values in a small area.

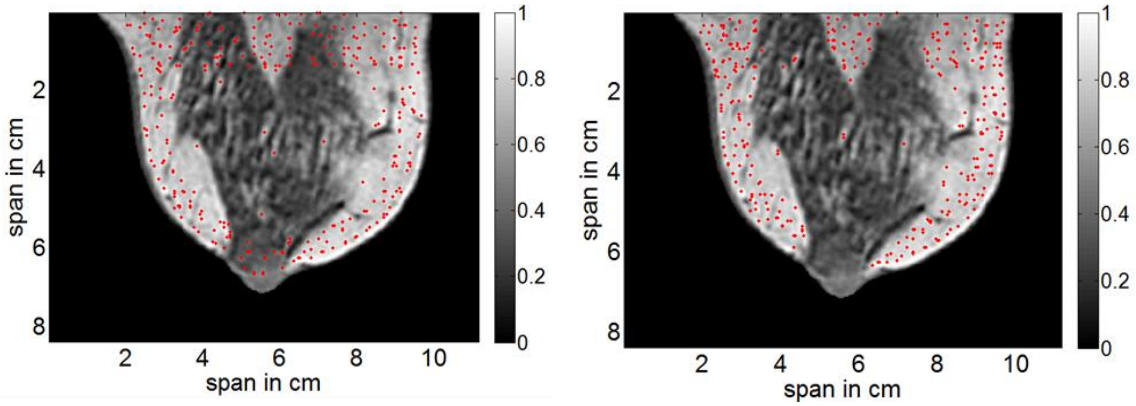

(a) (b)

Figure 3.14 : An illustration of discarding the undesired non-adipose sample voxels from the corresponding slice.

Therefore, to discard the non-adipose samples, again, I_{max} is scanned with a local window with different parameters for each of four regions. Corresponding window parameters used for reduction of sample points are given in Table 2. An intensity threshold operator p is applied inside the window to discard the voxels that are not satisfying the following condition:

$$i_{max}(r,c) > max(i_{max}) \,.\, p \qquad \textbf{(3.4)}$$

Here $i_{max}(r,c)$ denotes the retrieved point located at the coordinates (r,c) in a local window. The threshold operator p is selected as 0.85, which is also given in [45].

An example of discarding process is shown in Fig. 3.14 (b). As seen in (a), plenty of samples are collected from glandular tissue especially in the regions R2 and R3. These undesired samples belonging to non-adipose tissue are removed from the

corresponding slice as illustrated in (b). Now these samples belonging to adipose tissue can be used to estimate the bias field.

Table 3.2 : Corresponding window sizes for trimming out the non-adipose samples.

R_1	R_2	R_3	R_4
$n_{r1}=8N_r/25$	No Reduction	$n_{r3}=3N_r/25$	$n_{r4}=8sN_r/25$
$n_{c1}=8N_c/25$		$n_{c3}=3N_c/25$	$n_{c4}=8sN_c/25$
$o_{r1}=0.5n_{r1}$		$o_{r3}=0.5n_{r3}$	$o_{r4}=0.5n_{r4}$
$o_{c1}=0.5n_{c1}$		$o_{c3}=0.5n_{c3}$	$o_{c4}=0.5n_{c4}$

3.2.3 Removing the bias field and results

In order to model the bias field, an interpolated smooth surface is fitted to the sample voxels using thin plate smoothing. Thin plate smoothing spline surface fitted to the sample voxels is shown in Fig. 3.15(a) with a 3-D plot. As seen, the surface smoothly changes interpolating the sample voxels and lies through the whole slice. Since all

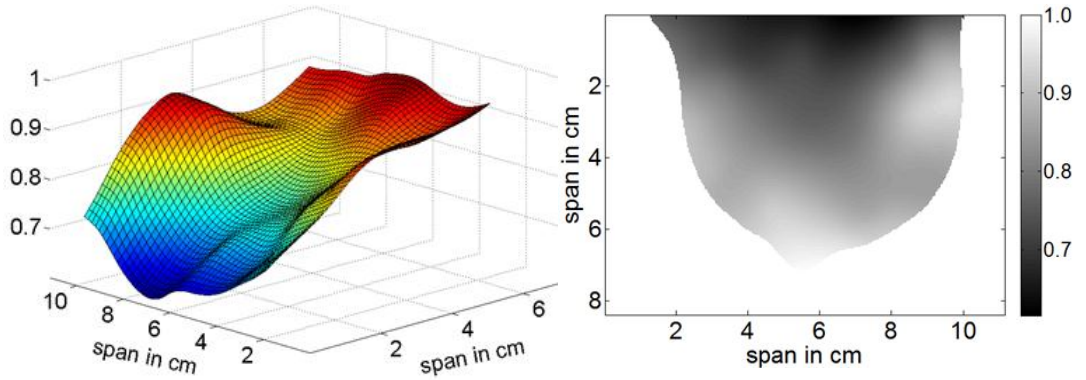

(a) (b)

Figure 3.15 : Bias field estimation using thin plate splines fitted to the sample points.

the samples are selected inside the breast and there are no samples selected from the background, estimated surface must be expected to be valid only inside the breast area. Therefore, the values which correspond to the background are rounded to 1 to obtain the bias field shown in Fig. 3.15(b).

Estimated bias field is removed from the corresponding slice by an element-wise division given below:

$$I_{corrected} = \frac{I_{orj}}{I_{bias}} \quad \textbf{(3.5)}$$

where I_{orj}represents the original voxel value disrupted by bias field, I_{bias} represents the bias fied estimated at the same location, and $I_{corrected}$ represents the corrected voxel value after bias field is eliminated. Fig. 3.16(a) shows the MRI slice corrupted with a disruptive bias field and the resultant slice after removing the bias field. As seen in (b), presented method for bias field elimination corrects the shadowing on the

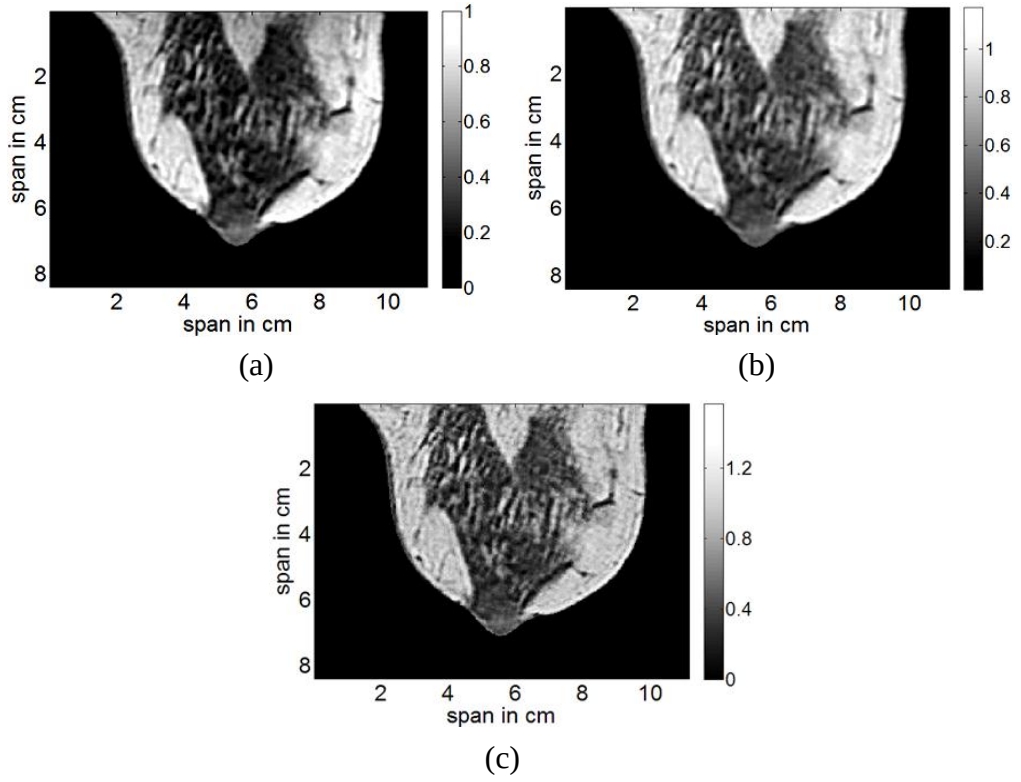

Figure 3.16 : Result of bias field elimination. (a)MRI slice corrupted with a disruptive bias field, and (b) the resultant slice after removing the bias field.

upper side of the slice as well as the undesired illumination on the boarders. Additionally, the contrast between glandular and adipose tissues is enhanced, by filtering the corresponding slice with an unsharp filter [42], [43] as depicted in (c).

Bias field correction also enhances the MRI histogram, uncovering the natural structure of the voxel intensity distribution of the breast tissue. Fig. 3.17 shows bias field correction results on various breast MRI data and corresponding histograms. The first and the second columns show pre-processed MRI data (background noise is eliminated) and the same slice after bias field correction. As the same, the third and

the fourth columns represent the histogram of the pre-processed MRI data and the same histogram after bias field correction respectively.

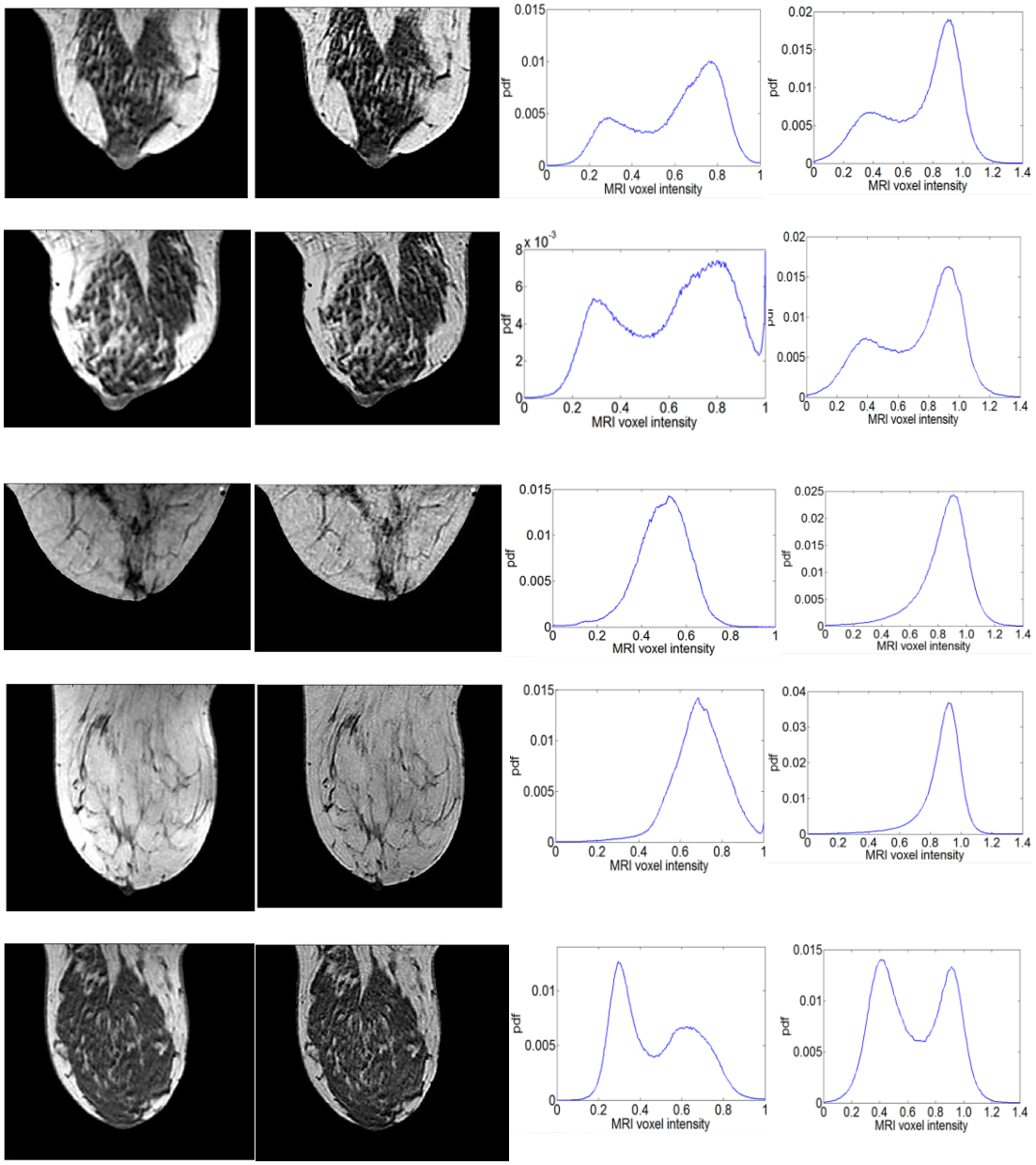

Figure 3.17 : Bias field correction results on various breast MRI data and corresponding histograms.

Fig. 3.18 shows the comparison between the slices denoised by homomorphic filtering and proposed method. First column shows different slices from different MRI data which are corrupted by bias field. Slices in the second column illustrate the resultant slices after homomorphic filtering. As seen, homomorphic filter reduces the background illumination, but obviously fails on the darker regions. On the other hand, bias field estimation and correction method presented in this study, corrects the

brighten regions reducing the illumination and also enhances the darker regions as well.

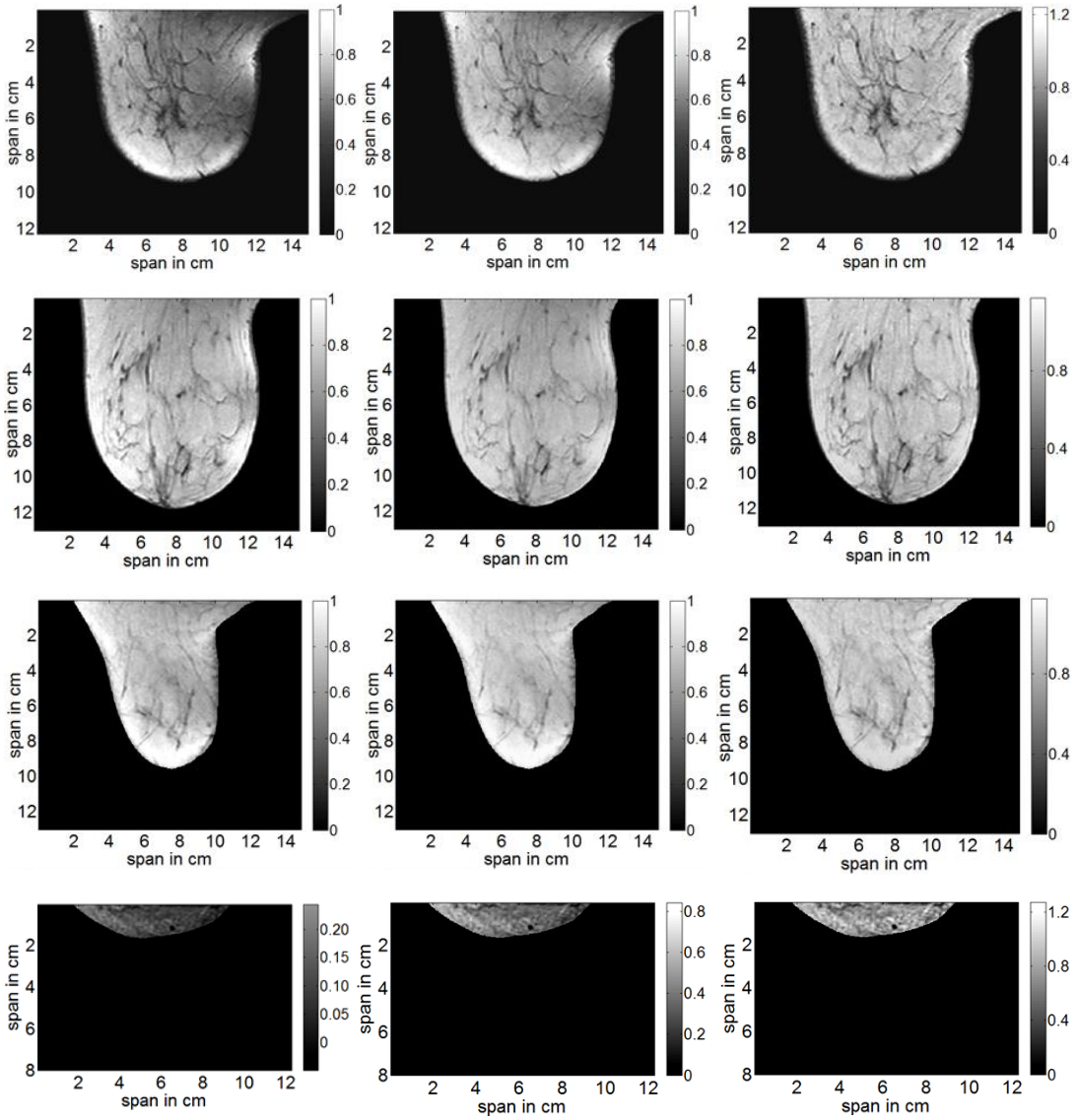

Figure 3.18 : Comparison between the slices denoised by homomorphic filtering and the presented method for bias field correction.

3.3 Segmentation of Two Main Tissues

Breast tissue composes of adipose, which gives the breast its shape and preserve protection, and glandular tissue that includes lobs, lobules and milk ducts. These two main tissues have different electromagnetic properties. Therefore, they must be separated on the MRI voxel intensity space, in order to assign correct electromagnetic properties according to their voxel intensities. Histogram of 3-D MRI breast data is assumed to consist of two Gaussian distributions of voxel

intensities representing glandular and adipose tissue distributions. In the previous study on 3-D breast phantoms [32], Gaussian Mixture Model (GMM) is used for segmentation of breast tissues. However, glandular and adipose tissues are well separated by GMM only if the considered breast is dense enough. In fatty breasts case (ACR 1 and some of ACR 2) as depicted in Fig. 3.19, upper bound of glandular tissue cannot be determined since the distribution belonging to the glandular tissue (blue curve) lies under the curve belonging to the adipose tissue (red curve).

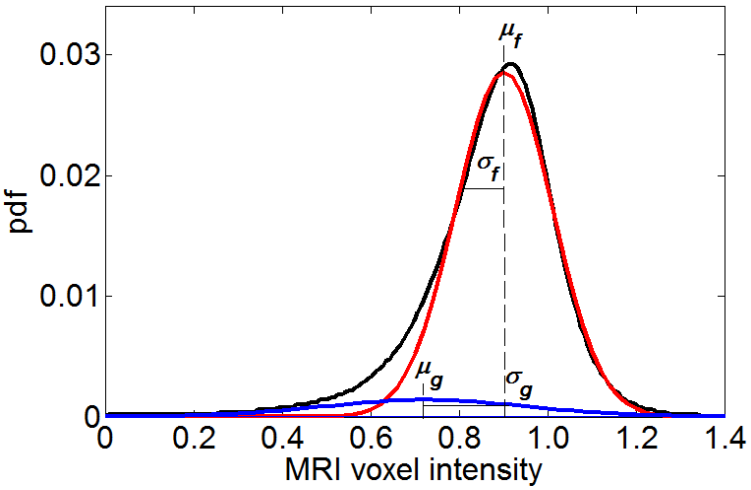

Figure 3.19 : Result of GMM on an almost entirely fatty breast.

Consequently, a different kind of segmentation method that is effective on all types of breasts is needed. In this study, a histogram based segmentation method, which determines a proper threshold value for separating glandular, and adipose tissues, is presented. The method is also based on the general characteristics of the histogram of breast MRI, but this time the purpose is to find the Gaussian distribution of adipose tissue. For breasts classified as ACR IV and most of ACR III, peaks of the Gaussian curves can be distinguishable on the histogram with the smaller peak at the left of the bigger one as illustrated in Fig. 3.20(a). However, as depicted in (b), for ACR I and ACR II type breasts, distribution of voxels intensities belong to glandular tissue does not exhibits a Gaussian like shape and any peak.

In brief, for a T1-weighted MRI histogram, glandular tissue may not preserves enough signs. However, a peak belongs to adipose tissue always exists so as its Gaussian shape above the Full Width Half Maximum (FWHM). Therefore, the parameters of the Gaussian distribution belong to the adipose tissue voxels in the

histogram can be determined by its FWHM property. A threshold value which correctly separates two tissue types must ensure that the distribution of adipose voxel intensities after segmentation must have nearly the same FWHM value which is 2.34 times of the standard deviation (σ_f) of itself.

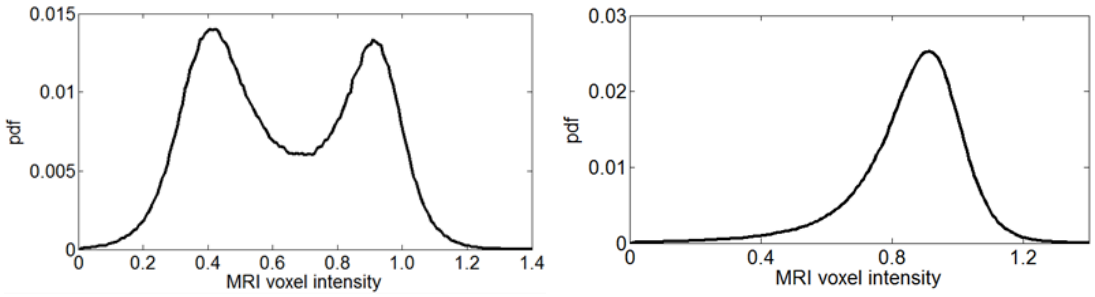

(a) (b)

Figure 3.20 : Histograms of two different breasts of different radiographic densities.

Let X be the set of voxel intensities in the breast interior and $f(x)$ is the probability density function of X. If the threshold value T, which separates two tissue types is defined then the standard deviation of the adipose tissue voxels can be found as

$$\sigma_f = \sqrt{\sum_{x>T} f(x)\left(\mu_f - x\right)^2} \qquad \textbf{(3.6)}$$

where μ_f is the expected value of the adipose tissue voxels. Then the threshold value that separates two tissue types can be calculated as below:

$$T = \underset{T \in X}{argmin}\ (|FWHM - 2.34\sigma_f|) \qquad \textbf{(3.7)}$$

FWHM of adipose tissue in a given histogram is calculated as the width of the distribution around the half of the peak that exists at higher voxel intensities. Before the segmentation process, in order to increase the consistency of calculated FWHM, histograms are smoothed by a moving average filter as depicted in Fig. 3.21. The length of the filter kernel is selected as three elements along the voxel intensity axis.

Segmentation results for various breasts are illustrated in Fig. 3.22 and 3.23. Both the visual results and the results in the histograms are given with different breast types. In Fig. 3.22, fitted Gaussian curves to the histograms of the breast classified into

different radiographic densities are illustrated to show the effectiveness of the segmentation procedure. Sub figures labeled as (a) to (d) represents the segmentation results of ACR class I to IV type breasts respectively. Red curves represent fitted Gaussian to the adipose distribution of tissue. Blue curves are calculated after finding the threshold value to represent how the rest of the distribution (which represents glandular tissue) behaves as a Gaussian distribution with parameters μ_g and σ_g. These two parameters are calculated as below:

$$\mu_g = \sum_{x=0}^{T} xf(x) \tag{3.8}$$

$$\sigma_g = \sqrt{\sum_{x>T} f(x)\big(\mu_g - x\big)^2} \tag{3.9}$$

Where μ_g and σ_g represents expected value and standard deviation of glandular tissue voxels respectively.

In addition, Fig. 3.23 shows the visual segmentation results on MRI slices of each of four ACR classes. Obviously, presented method succeeds in separating adipose and glandular tissues in MRI data for different breast characteristics

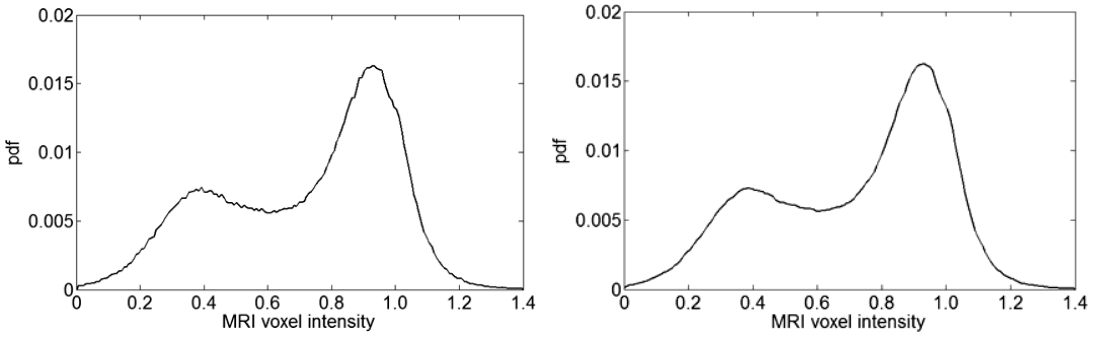

(a) (b)

Figure 3.21 : Smoothing the histogram by a moving average filter.

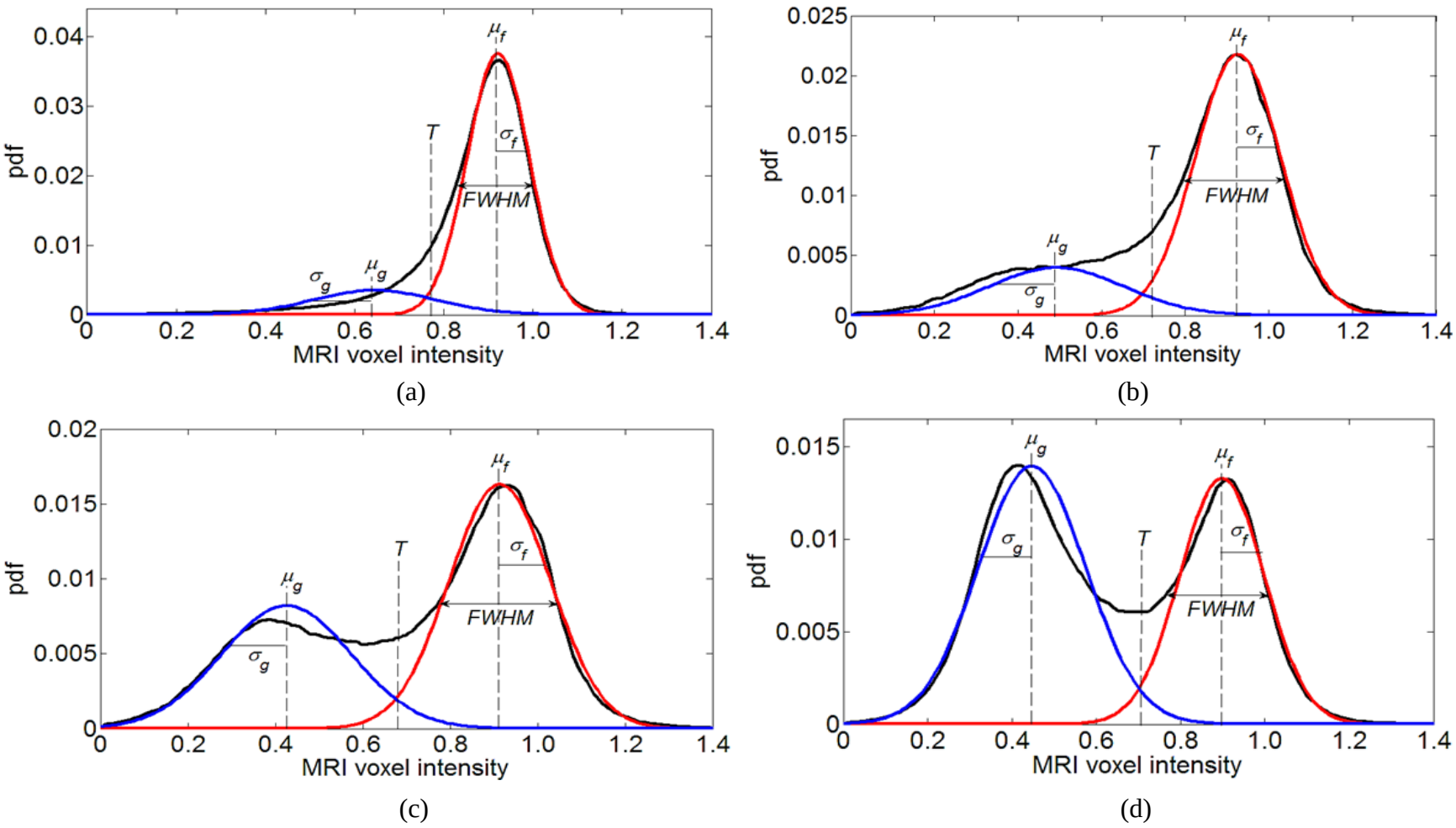

Figure 3.22 : Segmentation results on the histograms of the breast classified as different radiographic densities.

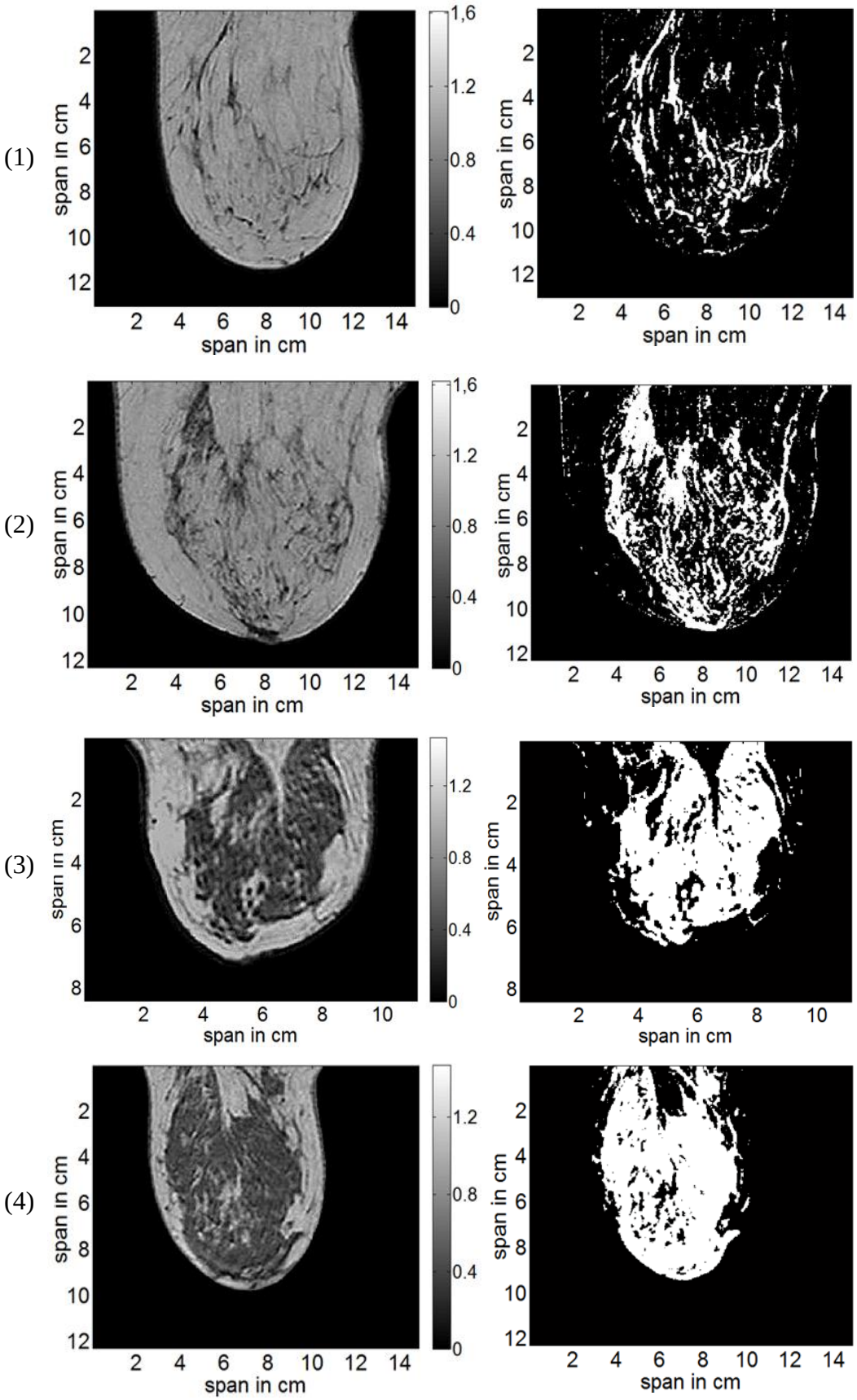

Figure 3.23 : Visual results of segmentation of the breast classified as different radiographic densities.

3.4 Electromagnetic Properties Mapping

Electromagnetic properties of breast tissue can be assigned to the corresponding voxel intensities in an MRI data via a proper nonlinear mapping function. In previous section breast tissue is separated into two main tissues in MRI data according to the corresponding voxel intensities. Similarly, adipose and glandular tissues have different electromagnetic properties. Dielectric properties of the breast tissue are revealed with a significant heterogeneity in Wisconsin–Calgary studies [13], [14]. In those studies, breast tissue are categorized into three groups according to the portion of adipose content and the maximum and minimum dielectric values for the breast found during the measurements.

Average values of relative permittivity (ε_r) and conductivity (σ) for tissue group 1 (0-30% adipose content) group 2 (31-84% adipose content), and group 3 (85-100% adipose content), as well as the maximum and minimum bounds, are calculated using the single-pole Cole-Cole model given in Table 3.

Table 3.3 : Parameters of single-pole Cole-Cole model for the five tissue groups.

Media	Electromagnetic Media Characteristics				
	ε_∞	$\Delta\varepsilon$	σ_s (S/m)	τ(ps)	α
maximum	1.000	66.31	1.370	7.585	0.063
group 1	7.821	41.48	0.713	10.66	0.047
group 2	5.573	34.57	0.524	9.149	0.095
group 3	3.140	1.708	0.036	14.65	0.061
minimum	2.293	0.141	0.002	16.40	0.251

Each of five tissue group represented by p_{max}(maximum), p_1(group 1), p_2(group 2), p_3(group 3), and p_{min}(minimum), for ε_r, and c_{max}(maximum), c_1(group 1), c_2(group 2), c_3(group 3),and c_{min}(minimum), for σ. Intervals between each group and/or maximum and minimum values are considered as four different intervals of dielectric properties of the breast. Fig. 3.24 shows the frequency dependence of single-pole Cole-Cole model for σ and ε_r. Four intervals of dielectric properties

labeled as $C1, C2, C3, C4$, and $P1, P2, P3, P4$, correspond to the four sub-categories of the breast tissue.

In MRI voxel intensity space, those four sub-categories are labeled with I_1, I_2, I_3,and I_4. They are defined by five intensity boundaries defined by I_{min}, $I_{\mu g}$, I_T, $I_{\mu f}$, I_{max} as depicted in Fig. 3.24. Minimum and maximum values of the dielectric properties are paired with I_{min} and I_{max}. Dielectric properties of group 1, group 2, and group 3

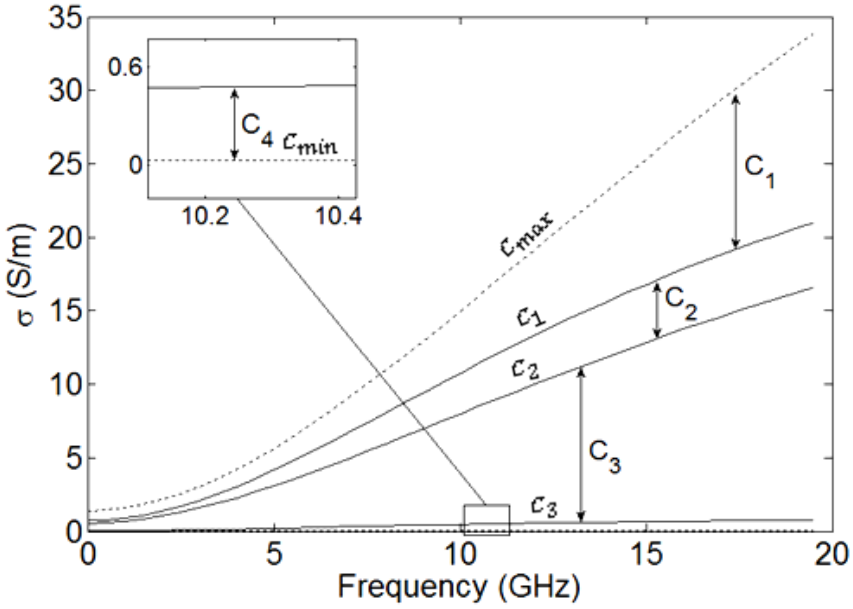

(a)

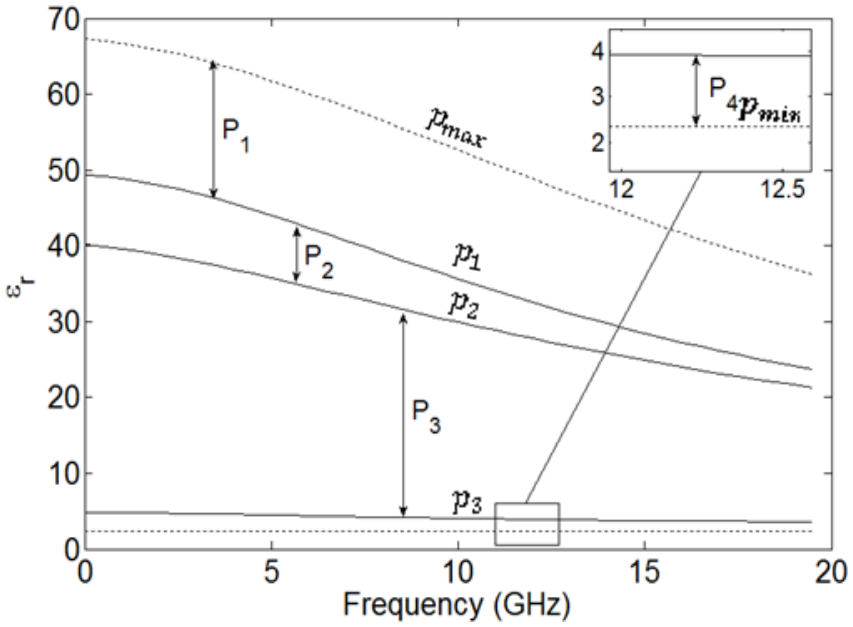

(b)

Figure 3.24 : Frequency dependence of single-pole Cole-Cole model for $\boldsymbol{\sigma}$ and $\boldsymbol{\varepsilon_r}$.

are related with $I_{\mu g}$, I_T, and $I_{\mu f}$, respectively. Five intensity boundaries are defined as below:

$$I_{min} = \mu_g - 3\sigma_g \tag{3.10}$$

$$I_{\mu g} = \sum_{x=0}^{T} xf(x) \tag{3.11}$$

$$I_{\mu f} = \sum_{x=T}^{\infty} xf(x) \tag{3.12}$$

$$I_T = T \tag{3.13}$$

$$I_{max} = \mu_f + 3\sigma_f \tag{3.14}$$

where μ_g andμ_f are expected values and σ_g and σ_f are the standard deviations of adipose and glandular tissue respectively. For a given histogram of an MRI data in Fig. 3.25, four voxel intensity intervals are depicted with the five boundary parameters, and the distributions of two main tissues are illustrated as a mixture of two Gaussians. Black curve represents the pdf of the voxel intensities in an MRI data. Dashed and dotted curves represent the glandular and adipose tissue distributions, respectively. For a specific operating frequency, if four intervals of electromagnetic properties are defined with five boundary points given as p_{max}, p_1, p_2, p_3, and p_{min}, for ε_r, and c_{max}, c_1, c_2, c_3,and c_{min}, for σ, then the intersections of those with eight MRI voxel intensity boundaries tell us how the mapping functions behave. For example, eight intersection points, (I_{min}, p_{max}), ($I_{\mu g}$, p_1), (I_T, p_2), ($I_{\mu f}$, p_3), (I_{max}, p_{min}), can be linearly connected each other to define a piece-wise linear mapping function for ε_r, considering the dielectric properties of each of four tissue types are linearly related with MRI voxel intensity values on their own interval. Alternatively, a non-linear interaction can be defined between those intervals preserving a more versatile relationship. Monotone piecewise polynomial cubic Hermite interpolation is used to form a nonlinear mapping function passing through five intersection points for ε_r and σ [38]-[39]. Nonlinear mapping functions should assure the following features:

1) It should be a monotonically decreasing function: Because higher intensities refer to tissues rich in adipose content, there is an inverse proportion between the MRI intensities and the dielectric properties. Monotone piecewise polynomial cubic Hermite interpolation ensures that the mapping functions is strictly monotonic.

2) It should cover the whole voxel intensity space in MRI data: Upper and lower bounds of mapping function in MRI voxel intensity axis is taken as $I_{min}$and I_{max} respectively. For voxel intensities greater than I_{max} are mapped to the minimum dielectric values, while the voxel intensities smaller than I_{min} are mapped to the maximum dielectric values.

An example of nonlinear mapping functions for both relative permittivity and conductivity are illustrated in Fig. 3.26. Each voxel in MRI data is mapped to appropriate electromagnetic properties through the non-linear mapping functions.

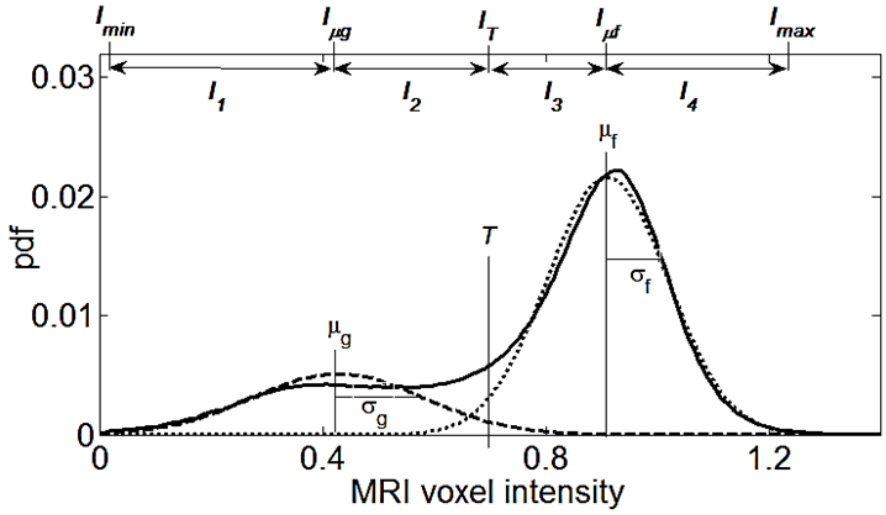

Figure 3.25 : Illustration of four voxel intensity intervals according to the distributions of two main tissues.

3.5 Building the 3-D Structure of Numerical Model

After mapping the electromagnetic properties to the MRI voxel intensities, slices in MRI data is linearly interpolated to form a proper volume. Interpolation process can be easily shown in coronal slices, which are depicted in Fig. 3.27. Normally, as mentioned before, MRI data consists of 40-45 axial slices which can also be shown as coronal slices by being stuck together as shown in (a).

Actually in z and x axes,MRI data consists of 300x300 voxels on average, but only 40-45 voxels in y direction. Dimensions of the voxels were given as 0.369mm x

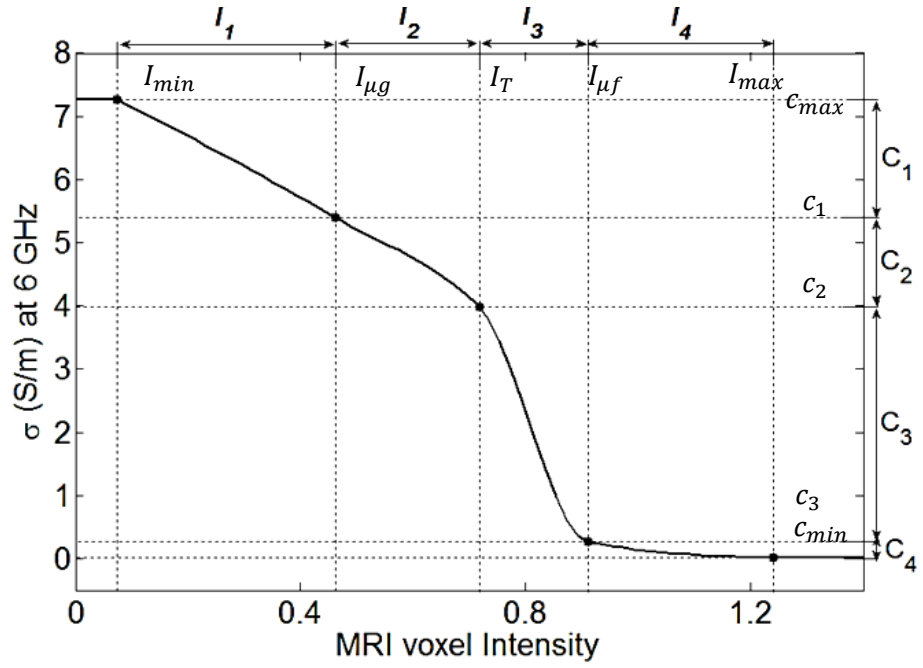

(a)

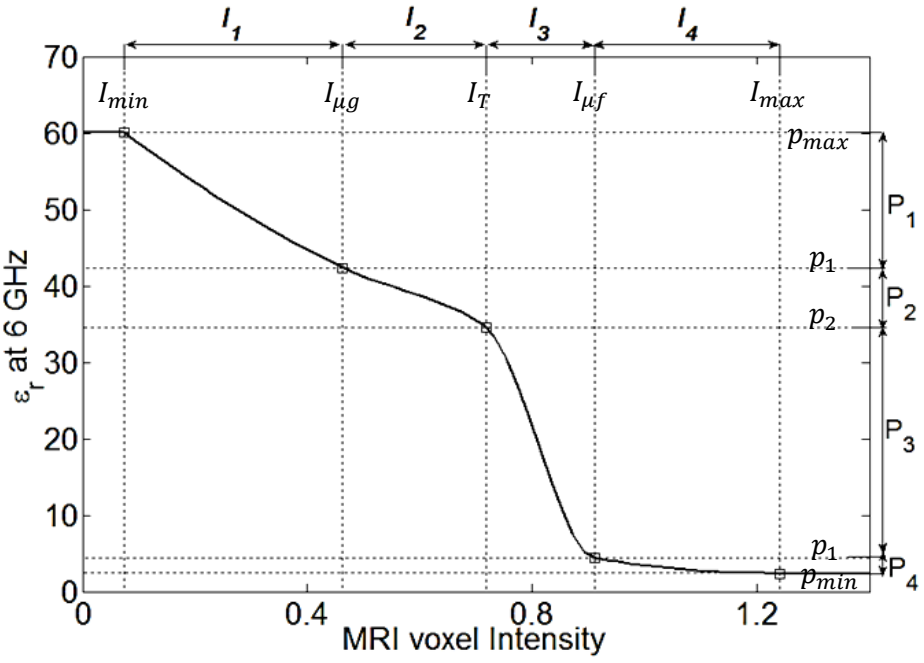

(b)

Figure 3.26 : Illustration of nonlinear mapping functions for both relative permittivity and conductivity.

0.369mm x 3mm in x, z and y dimensions respectively in Section 3.1 before. However, voxels are expected to be in cubic shape. Therefore, the interpolant i,

which is the parameter determining how the data is going to be stretched along y dimension, is calculated below:

$$i = \frac{3}{0.369} \cong 8.1 \qquad \textbf{(3.15)}$$

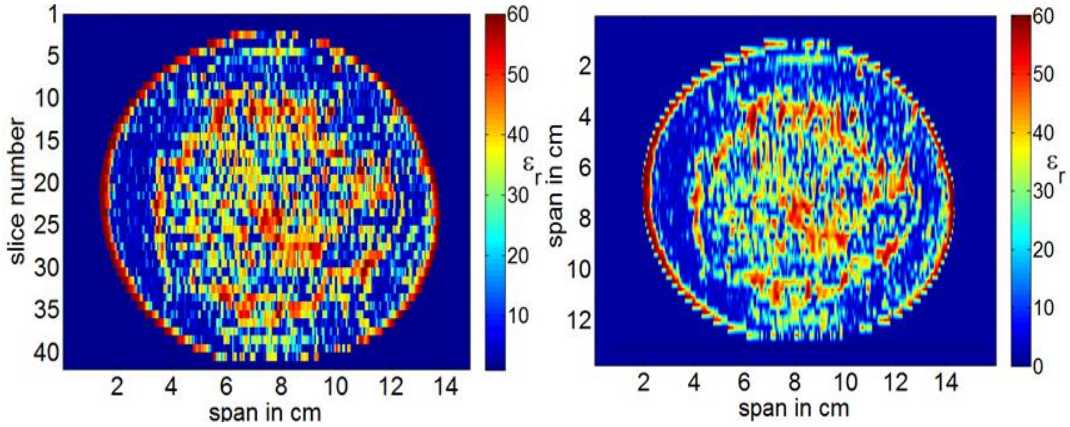

(a) (b)

Figure 3.27 : Illustration of linear interpolation on a coronal slice.

Linear interpolation produces the basis 3-D structure of numerical breast phantoms as illustrated in Fig. 3.28 (a). The basis structure is used to produce realistic breast shape for corresponding phantom. First, some additional slices that composed of entirely fat are added to the basic structure to maintain curvature of the breast surface as illustrated in (b).

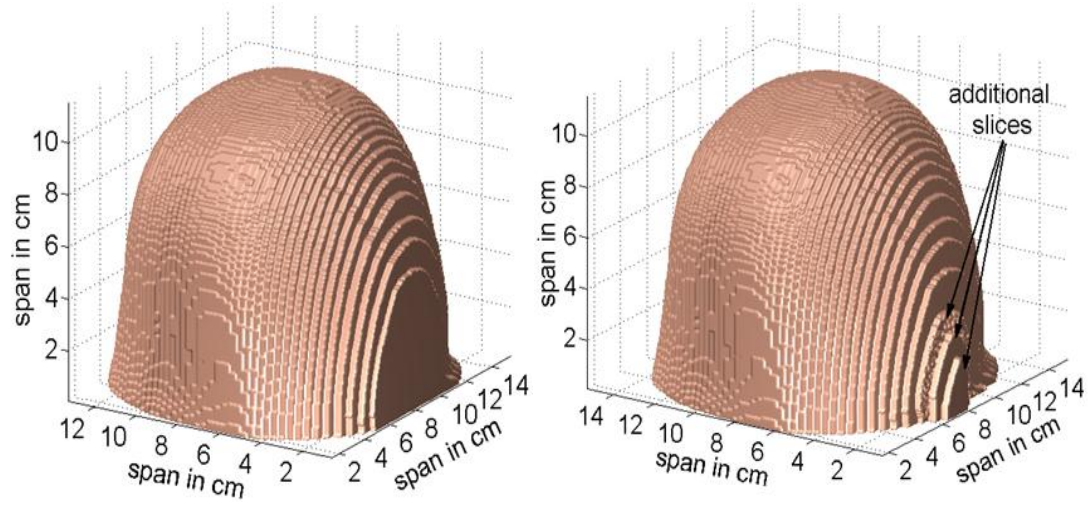

(a) (b)

Figure 3.28 : Representation of the basis structure and the additional slices.

The first and the last slices in the data is eroded by a rectangular binary structural element s. The length of s along z and x dimensions are called z_s and x_s respectively. They are defined by the difference in size between the last two adjacent slices. As shown in Fig. 3.29 below, z_s is taken as the size difference along z axis between two representative adjacent slices labelled as "slice a" and "slice b". The difference along x axis between the bottom rows of two adjacent slices is represented by x_{s1} and x_{s2} from each side. Accordingly, x_s is calculated as the arithmetic mean of x_{s1} and x_{s2}. As a result of linear interpolation, the surface of the structure looks like stair steps. This phenomenon, which appears around the edges of the structure in the direction of interpolation, is called stair step artifact. Structural deficits caused by this artifact disrupt the surface of the phantom yielding an unrealistic structure. Therefore, these deficits must be removed from the model in order to achieve a realistic smooth breast surface.

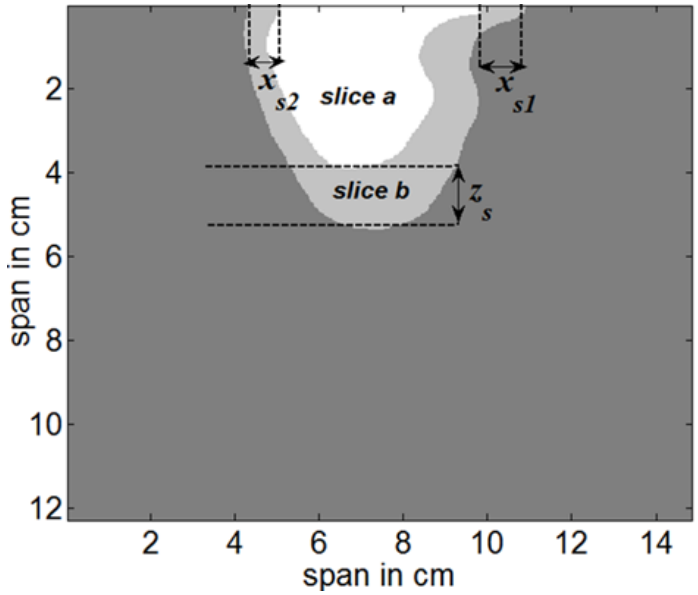

Figure 3.29 : Representation of the parameters used for generating the binary structural element.

It must be stated here that, the skin is not imaged accurately by MRI, and its remnants must be also removed from the model for accurate distribution of the dielectric properties. Therefore, both the skin and the structural deficits must be removed from the model at the same time using a 3-D Gaussian filter. First, a 3-D binary mask is generated for the interpolated data to reveal the edges and the corruptions on the surface. Then a 3-D Gaussian filter is applied to the surface of the

binary mask. Smoothed 3-D binary mask is visualized in Fig. 3.30 below. It is seen that, a Gaussian filter with a kernel size of 10 mm and a variance of 15 mm is quite enough to eliminate the stair step artifact.

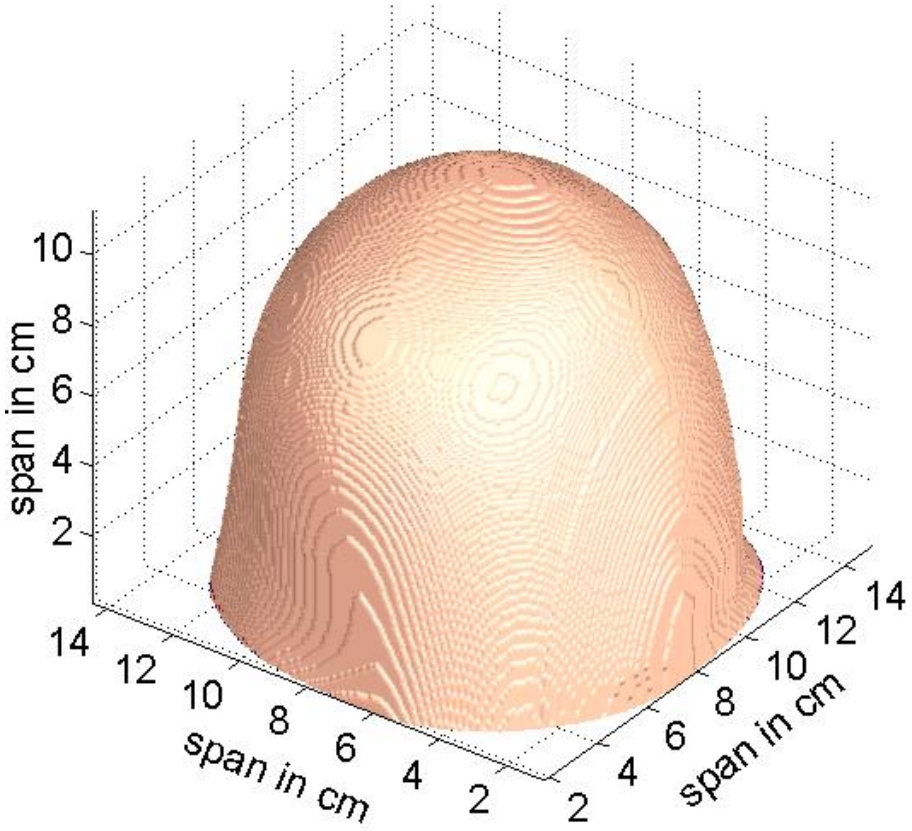

Figure 3.30 : Visualization of smoothed 3-D binary mask**.**

Smoothed mask is eroded to by 2.7 mm which is the maximum breast skin thickness given in [35]. Finally, interpolated data is masked with the smoothed and eroded binary mask to remove the stair step artifacts as well as the skin remnant. Fig. 3.31 (a) shows a coronal slice of an interpolated breast MRI data with skin remnant and stair step artifact around the edges. As shown in (b), the stair step artifact and the skin are eliminated at the same time by masking operation. The breast surface is dilated and covered by an artificially produced 1.5mm thick skin layer as depicted in (c).

Thickness of the skin layer is chosen to be the average value given in [35]. Whole structure is placed on an artificial chest model with a 1.5cm-thick subcutaneous fat followed by a 0.5cm thick muscle layer as depicted in Fig. 32. Dielectric properties of skin and muscle are obtained from the previous study reported Gabriel et al. [9].

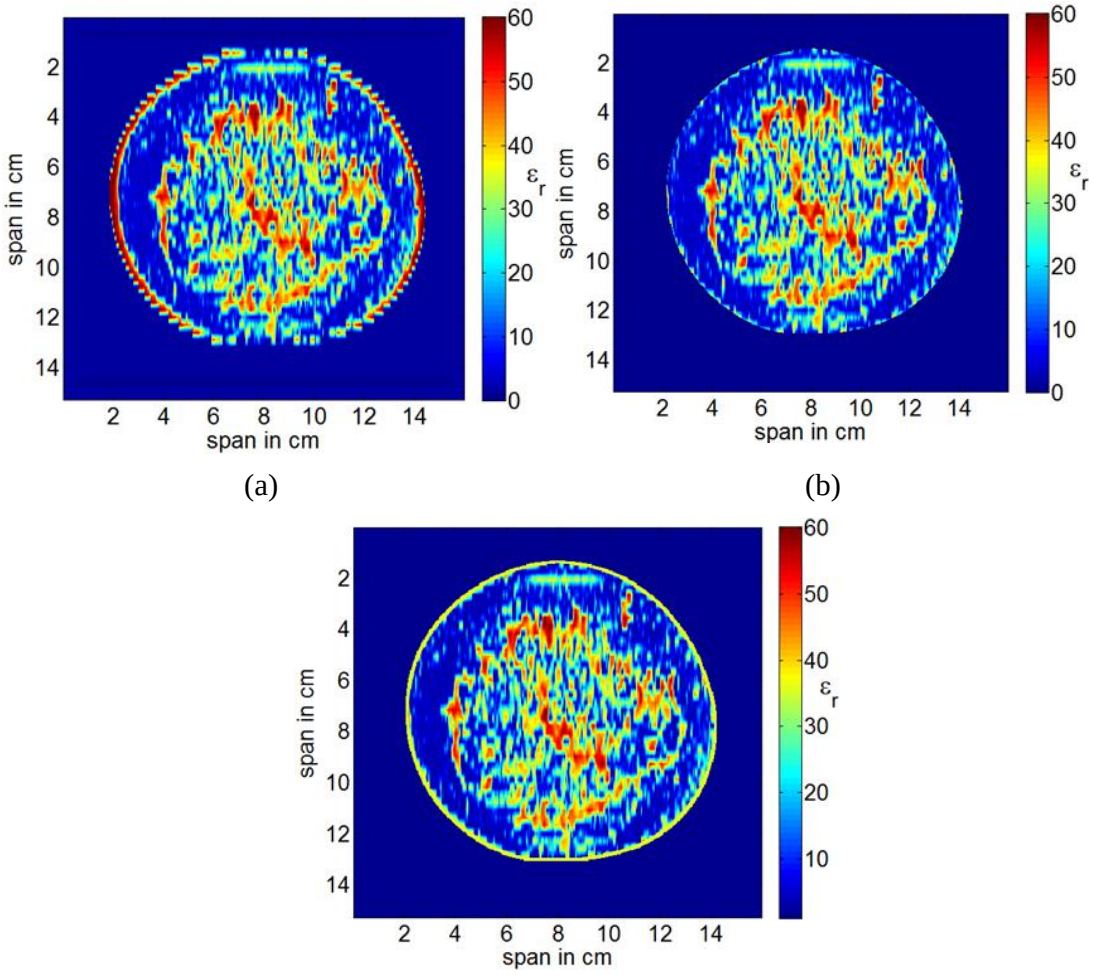

Figure 3.31 : Illustration of the stair step artifact and the skin remnant elimination and artificially produced skin layer.

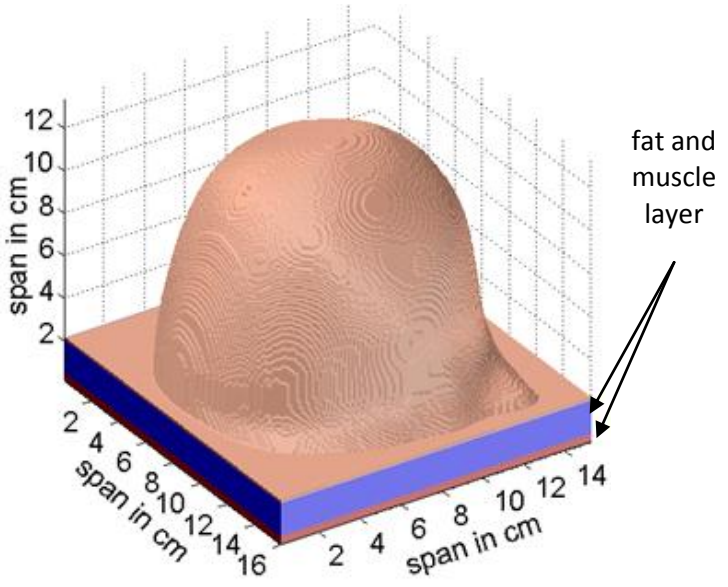

Figure 3.32 : Representation of artificially produced chest model.

For a desired frequency, dielectric properties of skin and muscle are determined using the single-pole Debye dispersion parameters given in Table 4.

Table 3.4 : Debye parameters for the dispersive materials used for the artificial muscle and skin layers.

Media	Electromagnetic Media Characteristics			
	ε_∞	$\Delta\varepsilon$	σ_s (S/m)	τ(ps)
muscle	4.00	50.00	1.370	7.23
skin	4.00	37.00	1.10	7.23

4. RESULTS

Realistic 3-D microwave breast phantoms with a broad variety were developed to be used in microwave breast cancer detection studies using T1-weighted 3-D MRI data of the patients in prone position. Each voxel intensity value in MRI data was mapped to the proper electromagnetic properties using the nonlinear mapping functions explained in Section II-D. For each numerical model, two different volume data (One for ε_r and the other for σ) representing both the spatial information and electromagnetic properties were produced. Since there is not a general method for classifying the breast MRIs according to its density, a methodology is presented to classify the numerical breast phantoms into four ACR categories according to the adipose tissue percentage in MRI data. Based on the threshold value T, the proportion of adipose tissue d in the corresponding data is calculated as:

$$d = \frac{\sum_{x=T} f(x)}{\sum f(x)} \tag{4.1}$$

Then the phantom is classified into one of the four ACR categories using the following rule:

$$ACR = \begin{cases} I, d > 0.8 \\ II, 0.7 < d \leq 0.8 \\ III, 0.6 < d \leq 0.7 \\ IV, d \leq 0.6 \end{cases} \tag{4.2}$$

In Fig. 4.1, examples for each of four ACR categories are given to show the effectiveness of the presented method. Axial cross sections of 3-D numerical breast phantoms belonging to four ACR categories are illustrated to show the distribution of dielectric properties. The first column depicts the filtered MRI slice, and the second and the third columns illustrate the relative permittivity and conductivity distributions respectively, for 6 GHz. In the first column, colour bars indicates the voxel intensity range and the other ones show the dielectric distribution ranges. Figures in each row illustrate the breasts of different ACR categories. In (a) and (b),

presented numerical phantoms are derived from the breasts of ACR I and II respectively. These types of breasts contain less glandular tissue than the breasts classified as ACR III and IV, so they look like more bluish according to the color range presented.

On the other hand, axial slices of the microwave models derived from ACR III and IV type breasts illustrated in (c) and (d) respectively, look like in mixed colours of red and orange, because of their high glandular tissue contents. Also, artificial chest wall and the skin layer can be seen in all microwave models.

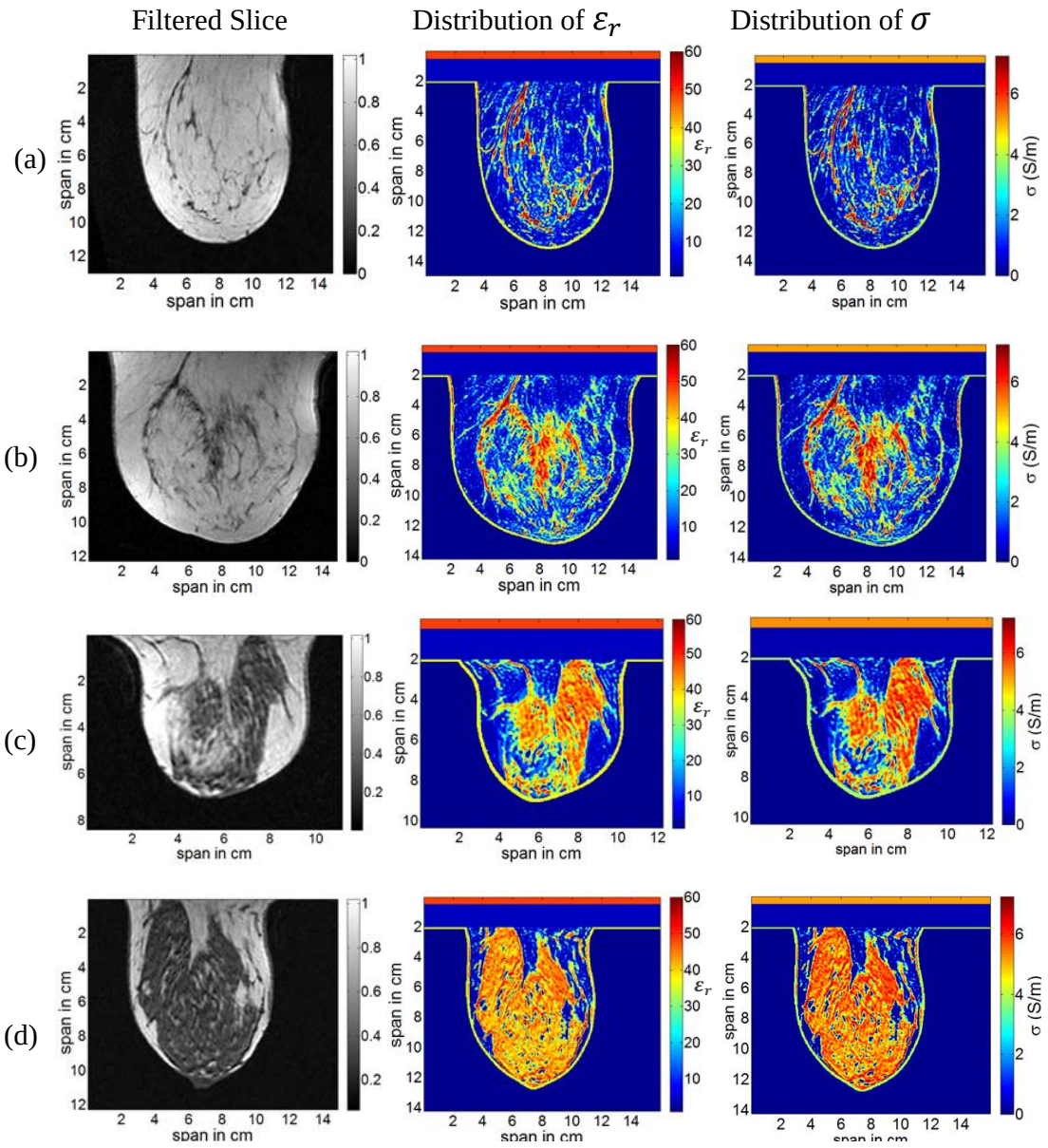

Figure 4.1 : 3-D numerical breast phantoms belonging to four ACR categories with axial cross sections showing the distribution of dielectric properties.

Also in Fig. 4.2, some examples of 3-D microwave breast models for 6 GHz. derived from the breast MRIs of different ACR classes are visualized to show the realistic shapes of the models. Sagittal cross-sections show the relative permittivity distributions and the color bars next to the figures show the relative permittivity variation.

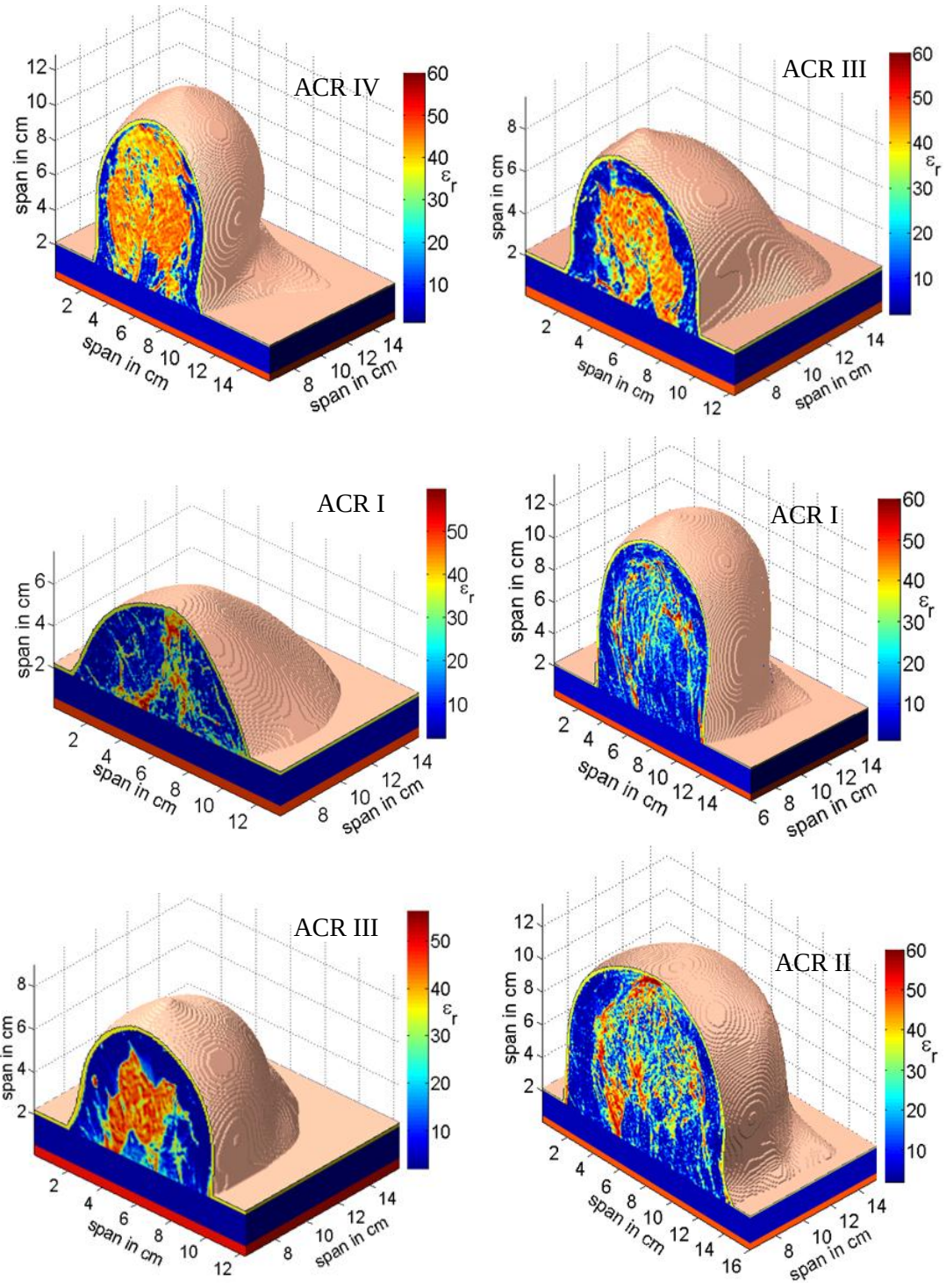

Figure 4.2 : Examples of 3-D microwave breast models belonging to different radiographic densities.

Any shape of tumor structures can be superimposed to the numerical phantoms for microwave breast cancer experiments. For a desired operating frequency, single pole Cole-Cole model can be used to calculate the dielectric properties of malignant tissue. Single pole Cole-Cole parameters for the malignant tissue are given in Table 5. Corresponding parameters are obtained from the Wisconsin-Calgary study [14].

Table 4.5 : Single-pole Cole-Cole model for the five dielectric property curves.

Media	Electromagnetic Media Characteristics				
	ε_∞	$\Delta\varepsilon$	$\sigma_s\ (S/m)$	$\tau(ps)$	α
tumor	6.749	50.09	0.794	10.5	0.051

Finally, the performance tests show that the proposed method can produce a phantom with 0.369 mm3 voxels in 5 to 15 minutes based on the breast size, on a 2.2 GHz Quad-Core system in MATLAB.

5. CONCLUSIONS AND RECOMMENDATIONS

In this study, realistic 3-D microwave breast models for microwave breast cancer detection and treatment studies were developed with a broad variety using T1-weighted MRI data of the patients in prone position. A general methodology which can be successfully applied any types of breast belonging to four ACR categories was presented. Each voxel intensity value in MRI data was mapped to the proper electromagnetic properties. Three main stages of numerical microwave phantom development process, presented in the literature, were re-arranged and enhanced to produce a better methodology.

First, an effective noise reduction technique which is based on estimating the bias field in breast MRI slices was presented. By this way, disorder of the intensity values belonging to glandular and adipose tissues are corrected. It was seen that, removing the bias field form the data, enhances the distribution of the voxel intensities, so that the natural shape of the histogram-mixture of two Gaussian curves- are revealed which is important for segmentation.

Second, an effective histogram based segmentation method for T1-weighted breast MRIs of different ACR classes was proposed for development of microwave breast phantoms. With the given segmentation method, development of microwave breast models was transformed into an autonomous process. Human dependency of the previous methods were substantially eliminated allowing to easily develop numerous numerical breast phantoms with various types for such studies in which plenty of different phantoms are required, such as neural networks algorithms.

Additionally, in contrast to uniform, piecewise linear and bimodal mapping methods, which were presented in previous studies, a non-linear mapping technique which assume a nonlinear transition between different tissues is presented for the first time.

With the presented method in this study, 3-D microwave breast models with various types and shapes can be developed for breast cancer detection and therapy studies for

desired microwave frequencies. For different wavelengths, (so as the different grid sizes) microwave breast models can be linearly interpolated to increase or decrease the grid size. However, if the required grid size is greater than the MRI voxel size, then, interpolating the MRI data to the required grid size at the beginning would significantly reduce the process time. On the other hand, if the required grid size is smaller than the MRI voxel size, than leaving the interpolation process at the end would be a better approach.

6. ACKNOWLEDGMENT

I would like to acknowledge to technical assistance of the Euromed Medical Center and Marmara University Medical Faculty and in acquiring the breast MRIs and my colleagues for their contributions during this study.

REFERENCES

[1] **Ferlay J, Shin H.R., Bray F., Forman D., Mathers C. and Parkin D.M.,** *"Cancer Incidence and Mortality Worldwide,"* GLOBOCAN 2008 v2.0, IARC CancerBase, No. 10, Lyon, France: International Agency for Research on Cancer; 2010.

[2] **Jemal, A., Bray, F., Center, M. M., Ferlay, J., Ward, E. and Forman, D.,** "*Global cancer statistics,*" CA: A Cancer Journal for Clinicians, 61: 69–90. doi: 10.3322/caac.20107,2011.

[3] **How many different types of cancer are there? : Cancer Research UK : CancerHelp UK**., Date retrieved: 11 May 2012, Address: http://www.cancerresearchuk.org/cancer-help/about-cancer/cancer-questions/how-many-different-types-of-cancer-are-there

[4] **O'Halloran, M., Conceiçao, R., et.al.,** *"FDTD Modeling of the Breast: A Review,"* Progress In Electromagnetics Research B, Vol. 18, 1-24, 2009

[5] **Sylvia H. Heywang-Köbrunner, Astrid Hacker, et.al.,** "*Advantages and Disadvantages of Mammography Screening,*" Breast Care 2011, vol. 6, pp. 199–207, 2011. DOI:10.1159/000329005

[6] **Kösters JP, Gøtzsche PC.,** "*Regular Self-Examination or Clinical Examination for Early Detection of Breast Cancer,*" Cochrane Database of Systematic Reviews 2003, Issue 2. Art. No: CD003373.DOI: 10.1002/146518 58.CD003373.

[7] **Newman B., Mu H., et.al.,** "*Frequency of Breast Cancer Attributable to BRCA1 in a Population-Based Series of American Women,*" JAMA. 1998; 279:915–21.

[8] **Yaffe M.J., Mainprize J.G.,** "Risk of Radiation-induced Breast Cancer from Mammographic Screening", Radiology, vol. 258, pp. 98–105, January 2011.

[9] **S. Gabriel, R.W. Lau, and C. Gabriel,** "*The Dielectric Properties of Biological Tissues: III. Parametric Models for the Dielectric Spectrum of Tissues,*" Phys. Med. Biol., vol. 41, pp. 2271–2293, 1996.

[10] **S. S. Chaudhary, R. K. Mishra, A. Swarup, and J. M. Thomas,** "*Dielectric Properties of Normal and Malignant Human Breast Tissues at Radiowave and Microwave Frequencies,*" Indian J. Biochem. Biophys., vol. 21, pp. 76–79, 1984.

[11] **A. J. Surowiec, S. S. Stuchley, J. R. Barr, and A. Swarup,** "*Dielectric Properties of Breast Carcinoma and the Surrounding Tissues,*" IEEE Trans. Biomed. Eng., vol. 35, no. 4, pp. 257–263, Apr. 1988.

[12] **W. T. Joines, Y. Zhang, C. Li, and R. L. Jirtle,** "*The Measured Electrical Properties of Normal and Malignant Human Tissues From 50 to 900 Mhz,*" Med. Phys. J., vol. 21, no. 4, pp. 547–550, 1994.

[13] **M. Lazebnik, L. McCartney, et.al.,** "*A Large-Scale Study of the Ultrawideband Microwave Dielectric Properties of Normal Breast*

Tissue Obtained From Reduction Surgeries," Phys. Med. Biol., vol. 52, pp. 2637–2656, 2007.

[14] **M. Lazebnik, D. Popovic, et.al.,** "*A Large-Scale Study of the Ultrawideband Microwave Dielectric Properties of Normal, Benign and Malignant Breast Tissues Obtained From Cancer Surgeries*," Phys. Med. Biol., vol. 52, pp. 6093–6115, 2007.

[15] **P. Meaney, M. W. Fanning, T. Raynolds, C. J. Fox, Q. Fang, C. A. Kogel, S. P. Poplack, and K. D. Paulsen,** "*Initial Clinical Experience With Microwave Breast Imaging in Women With Normal Mammography*," Acad. Radiol., vol. 14, no. 2, pp. 207–218, 2007.

[16] **A. Fhager, P. Hashemzadeh, and M. Persson,** "*Reconstruction Quality and Spectral Content of an Electromagnetic Time-Domain Inversion Algorithm*," IEEE Trans. Biomed. Eng., vol. 53, no. 8, pp. 1594–1604, Aug. 2006.

[17] **Z. Q. Zhang and Q. H. Liu,** "Three-dimensional nonlinear image reconstruction for microwave biomedical imaging," IEEE Trans. Biomed. Eng., vol. 51, no. 3, pp. 544–548, Mar. 2004.

[18] **X. Li, E. J. Bond, B. D. V. Veen, and S. C. Hagness,** "*An Overview of Ultrawideband Microwave Imaging Via Space–Time Beamforming for Early Stage Breast-Cancer Detection*," IEEE Antennas Propag. Mag., vol. 47, no. 1, pp. 19–34, Feb. 2005.

[19] **P. Kosmas and C. M. Rappaport,** "*FDTD-Based Time Reversal for Microwave Breast Cancer Detection—Localization in Three Dimensions*," IEEE Trans. Microw. Theory Tech., vol. 54, no. 4, pp. 1921–1927, Jun 2006.

[20] **Y. Chen, E. Gunawan, K. S. Low, S. Wang, Y. Kim, and C. Soh,** "*Pulse Design for Time Reversal Method as Applied to Ultrawideband Microwave Breast Cancer Detection: A Two-Dimensional Analysis*," IEEE Trans. Antennas Propag., vol. 55, no. 1, pp. 194–204, Jan 2007.

[21] **G. Ku, B. D. Fornage, X. Jin, M. H. Xu, K. K. Hunt, and L. V. Wang,** "*Thermoacoustic and Photoacoustic Tomography of Thick Biological Tissues Toward Breast Imaging*," Technol. Cancer Res. Treat., vol. 4, no. 5, pp. 559–565, 2005.

[22] **M. Elsdon, D. Smith,M. Leach, and S. J. Foti**, "*Experimental Investigation of Breast Tumor Imaging Using Indirect Microwave Holography*," Microw.Opt. Technol. Lett., vol. 48, no. 3, pp. 480–482, 2006.

[23] **R. A. Gardner, H. I. Vargas, J. B. Block, C. L. Vogel, A. J. Fenn, G. V. Kuehl, and M. Doval,** "*Focused Microwave Phased Array Thermotherapy for Primary Breast Cancer*," Ann. Surg. Oncol., vol. 9, no. 4, pp. 326–332, 2002.

[24] **H. I. Vargas, W. C. Dooley, R. A. Gardner, K. D. Gonzalez, R. Venegas, S. H. Heywang-Kobrunner, and A. J. Fenn,** "*Focused Microwave Phased Array Thermotherapy for Ablation of Early-Stage Breast Cancer: Results of Thermal Dose Escalation*," Ann. Surg. Oncol., vol. 11, no. 2, pp. 139–146, 2004.

[25] **Bansal, R.**,"Battling cancer: the latest on microwave hyperthermia," Microwave Magazine, IEEE , vol.6, no.3, pp. 32- 34, Sept. 2005

[26] **M. Converse, E. J. Bond, B. D. Van Veen, and S. C. Hagness,** "*A Computational Study of Ultrawideband Versus Narrowband*

Microwave Hyperthermia for Breast Cancer Treatment," IEEE Trans. Microw. Theory Tech., vol. 54, no. 5, pp. 2169–2180, May 2006.

[27] **Stang, J.; Haynes, M.; Carson, P.; Moghaddam, M.,** "*A Preclinical System Prototype for Focused Microwave Thermal Therapy of the Breast,"* Biomedical Engineering, IEEE Transactions on , vol.59, no.9, pp.2431-2438, Sept. 2012

[28] **S. C. Hagness, A. Taflove, and J. E. Bridges,** "*Two-Dimensional FDTD Analysis of a Pulsed Microwave Confocal System for Breast Cancer Detection: Fixed-Focus and Antenna-Array Sensors*," IEEE Trans. Biomed. Eng., vol. 45, pp. 1470–1479, Dec. 1998.

[29] **A. E. Souvorov, A. E. Bulyshev, S. Y. Semenov, R. H. Svenson, and G. P. Tatsis,** "*Two-Dimensional Computer Analysis of a Microwave Flat Antenna Array for Breast Cancer Tomography*," IEEE Trans. Microwave Theory Tech., vol. 48, pp. 1413–1415, Aug. 2000.

[30] **X. Li and S. C. Hagness,** "*A Confocal Microwave Imaging Algorithm for Breast Cancer Detection*,"IEEE Microwave and Wireless Components Letters, vol. 11, no. 3, pp. 130–132, 2001.

[31] **Converse, M. and et al.,** "*A Computational Study of Ultrawideband Versus Narrowband Microwave Hyperthermia for Breast Cancer Treatment*," IEEE Transactions on Microwave Theory and Techniques, Vol. 54, 2169-2180, 2006.

[32] **Zastrow, E., Davis, S. K., et.al.,** "*Development of Anatomically Realistic Numerical Breast Phantoms with Accurate Dielectric Properties for Modeling Microwave Interactions with the Human Breast*," IEEE Trans. on Biomedical Engineering, Vol. 55, No. 12, pp 2792-2799, 2008.

[33] **American College of Radiology,** Breast Imaging Reporting and Data System (BI-RADS) Atlas, 4th ed. Reston, VA: Amer. Coll. Radiol., 2003.

[34] **Osborne MP and Boolbol SK.,** "*Chapter 1: Breast anatomy and development*", in Harris JR, Lippman ME, Morrow M, Osborne CK. Diseases of the Breast, 4th edition. Lippincott Williams and Wilkins, 2010.

[35] **J. T. L. Pope, M. E. Read, T. Medsker, A. J. Buschi, and A. N. Brenbridge,** "*Breast Skin Thickness: Normal Range and Causes of Thickening Shown on Film-Screen Mammography,"* J. Can. Assoc. Radiol., vol. 35, pp. 365–368, 1984S. S. Chaudhary, R. K. Mishra, A. Swarup, and J.

[36] **J. Duchon,** 1976, "*Splines Minimizing Rotation Invariant Semi-norms in Sobolev Spaces*," pp 85-100, In: Constructive Theory of Functions of Several Variables, Oberwolfach 1976, W. Schempp and K. Zeller, eds., Lecture Notes in Math., Vol. 571, Springer, Berlin, 1977.

[37] **P. J. Green and B. W. Silverman.** "*Nonparametric Regression and Generalized Linear Models, A Roughness Penalty Approach,"* Chapman & Hall, 1994.

[38] **Fritsch, F.N. Carlson, R.E.,** "*Monotone Piecewise Cubic Interpolation*". SIAM Journal on Numerical Analysis, 17 (2): 238–246, 1980.

[39] **James M. Hyman,** "*Accurate Monotonicity Preserving Cubic Interpolation*", SIAM Journal on Numerical Analysis, vol. 4, No. 4, Dec. 1983.

[40] **M. J. Firbank, A. Coulthard, et.al.,** "*A Comparison of two Methods for Measuring the Signal to Noise Ratio on MR Images,"* Phys. Med. Biol., vol. 44, pp. N261–N264., 1999.

[41] **N. Otsu,** *"A threshold selection method from gray-level histograms,"* IEEE Trans. Sys., Man., Cyber. 9, pp. 62–66, 1979.
[42] **R. C. Gonzalez and R. E. Woods,** Digital Image Processing, 2nd ed. Upper Saddle River, NJ: Prentice-Hall, 2002.
[43] **R. M. Haralick and L. G. Shapiro,** Computer and Robot Vision, 1st ed. Boston, MA: Addison-Wesley, 1992.
[44] **John G. Sled and Alex P. Zijdenbos.,** "*A Nonparametric Method for Automatic Correction of Intensity Nonuniformity in MRI Data,*" IEEE Transactions On Medical Imaging, 17(1):87,97, 1998.
[45] **Jorgensen, F. S.** "*Segmentation of Male Abdominal Fat Using MRI*" Master's Thesis, Technical University of Denmark, Kongens Lyngby, Denmark. pp 11-35, 2006.
[46] **Breast Anatomy,** In Wikipedia. Date retrieved: 07.09.2012, Address: http://en.wikipedia.org/wiki/File:Breast_anatomy_normal_scheme.png.

CURRICULUM VITAE

Name Surname: Ahmet Hakan TUNÇAY

Place and Date of Birth: Eskişehir/Turkey - 04.07.1986

Address: Hafız Ata Sokak, Ayık Apt. No:5 Daire:6 Şişli/Mecidiyeköy İstanbul/Turkey

E-Mail: ahakantuncay@gmail.com

B.Sc.: Eskişehir Osmangazi University

M.Sc.: Istanbul Technical University

Professional Experience and Rewards:

- Spy 2008 Savronik Project Competition, Eskişehir/Turkey – 2nd Prize
  With the project: *Bomb Deactivator Robot; working with RF serial communication from a laptop*
- Spy 2009 Savronik Project Competition, Eskişehir/Turkey - 2nd Prize
  With the project: *Sky Intervention Vehicle; some kind of a helicopter that is working with RF serial communication from a laptop based on the images taken from the camera on the vehicle*
- Spy 2010 Savronik Project Competition, Eskişehir/Turkey - 2nd Prize
  With the project: *Design and control of a mobile robot using live image data taken from a stationary camera mounted at a stationary place*

List of Publications and Patents:

- A.H. Tunçay, P. Özmen, "An Image Processing Based Approach for Development of Anatomically Realistic Breast Phantoms with Accurate Dielectric Properties," 1st National EMC Conference, 14-16 September 2011, Doğuş University, İstanbul.
- A. H. Tunçay, İ. Akduman, "Nonlinear Mapping of Electromagnetic Properties to Breast Tissues Using T1-Weighted 3-D MRI Data," Progress in Electromagnetics Research Symposium Abstracts, Moscow, Russia, August 19-23, pp. 263, 2012.
- A.H. Tunçay, İ. Akduman, "Realistic Microwave Breast Models Through T-1 Weighted 3-D MRI Data", 2012 (Under Review).

PUBLICATIONS/PRESENTATIONS ON THE THESIS

- A. H. Tunçay, İ. Akduman, "Nonlinear Mapping of Electromagnetic Properties to Breast Tissues Using T1-Weighted 3-D MRI Data," Progress in Electromagnetics Research Symposium Abstracts, Moscow, Russia, August 19-23, pp. 263, 2012.